



# **NAVAL POSTGRADUATE SCHOOL**

**MONTEREY, CALIFORNIA**

## **THESIS**

**COASTAL BATHYMETRY USING 8-COLOR  
MULTISPECTRAL SATELLITE OBSERVATION OF  
WAVE MOTION**

by

Bradley L. McCarthy

September 2010

Thesis Advisor:  
Second Reader:

Richard C. Olsen  
Fred A. Kruse

**Approved for public release; distribution is unlimited**

THIS PAGE INTENTIONALLY LEFT BLANK

<b>REPORT DOCUMENTATION PAGE</b>			<i>Form Approved OMB No. 0704-0188</i>	
Public reporting burden for this collection of information is estimated to average 1 hour per response, including the time for reviewing instruction, searching existing data sources, gathering and maintaining the data needed, and completing and reviewing the collection of information. Send comments regarding this burden estimate or any other aspect of this collection of information, including suggestions for reducing this burden, to Washington headquarters Services, Directorate for Information Operations and Reports, 1215 Jefferson Davis Highway, Suite 1204, Arlington, VA 22202-4302, and to the Office of Management and Budget, Paperwork Reduction Project (0704-0188) Washington DC 20503.				
<b>1. AGENCY USE ONLY (Leave blank)</b>		<b>2. REPORT DATE</b> September 2010	<b>3. REPORT TYPE AND DATES COVERED</b> Master's Thesis	
<b>4. TITLE AND SUBTITLE</b> Coastal Bathymetry Using 8-Color Multispectral Satellite Observation of Wave Motion			<b>5. FUNDING NUMBERS</b>	
<b>6. AUTHOR(S)</b> Bradley L. McCarthy				
<b>7. PERFORMING ORGANIZATION NAME(S) AND ADDRESS(ES)</b> Naval Postgraduate School Monterey, CA 93943-5000			<b>8. PERFORMING ORGANIZATION REPORT NUMBER</b>	
<b>9. SPONSORING /MONITORING AGENCY NAME(S) AND ADDRESS(ES)</b> N/A			<b>10. SPONSORING/MONITORING AGENCY REPORT NUMBER</b>	
<b>11. SUPPLEMENTARY NOTES</b> The views expressed in this thesis are those of the author and do not reflect the official policy or position of the Department of Defense or the U.S. Government. IRB Protocol number _____.				
<b>12a. DISTRIBUTION / AVAILABILITY STATEMENT</b> Approved for public release; distribution is unlimited			<b>12b. DISTRIBUTION CODE</b>	
<b>13. ABSTRACT (maximum 200 words)</b>  Coastal bathymetry was measured using wave motion as observed by a commercial satellite imaging system. The linear finite depth dispersion relation for surface gravity waves was used to determine nearshore ocean depth from successive images acquired by the WorldView-2 satellite of the coastal area near Camp Pendleton, California. Principal component transforms were performed on co-registered images and principal component four was found to very effectively highlight wave crests in the surf zone. Change detection images, which included principal component four from successive images, contained both spatial and temporal information. From these change detection images, wave celerity could be determined and depth inversion could be performed. For waves farther from shore, principal component four no longer highlighted wave crests. Waves could be resolved within a single RGB composite image with equalization enhancement. The wavelength of a wave above a known depth was measured and the wave period method was used to determine depth for other waves in the propagation direction of this wave. Our depth calculations compared favorably to our reference bathymetry. The spatial resolution for this method of determining depth is higher and perhaps more accurate than our reference bathymetry, particularly in the surf zone.				
<b>14. SUBJECT TERMS</b> Remote Sensing, Multispectral, 8-Color, Bathymetry, WorldView-2, ENVI, Principal Component Transform, Depth Inversion, Wave Methods, Dispersion Relation.			<b>15. NUMBER OF PAGES</b> 71	
			<b>16. PRICE CODE</b>	
<b>17. SECURITY CLASSIFICATION OF REPORT</b> Unclassified	<b>18. SECURITY CLASSIFICATION OF THIS PAGE</b> Unclassified	<b>19. SECURITY CLASSIFICATION OF ABSTRACT</b> Unclassified	<b>20. LIMITATION OF ABSTRACT</b> UU	

NSN 7540-01-280-5500

Standard Form 298 (Rev. 2-89)  
Prescribed by ANSI Std. Z39-18

THIS PAGE INTENTIONALLY LEFT BLANK



**Approved for public release; distribution is unlimited**

**COASTAL BATHYMETRY USING 8-COLOR MULTISPECTRAL SATELLITE  
OBSERVATION OF WAVE MOTION**

Bradley L. McCarthy  
Civilian, Systems Engineer, The Boeing Company  
M.S., The Johns Hopkins University, 2003

Submitted in partial fulfillment of the  
requirements for the degree of

**MASTER OF SCIENCE IN REMOTE SENSING INTELLIGENCE**

from the

**NAVAL POSTGRADUATE SCHOOL  
September 2010**

Author: Bradley L. McCarthy

Approved by: Dr. Richard C. Olsen  
Thesis Advisor

Dr. Fred A. Kruse  
Second Reader

Dr. Dan C. Boger  
Chairman, Department of Information Sciences

THIS PAGE INTENTIONALLY LEFT BLANK

## **ABSTRACT**

Coastal bathymetry was measured using wave motion as observed by a commercial satellite imaging system. The linear finite depth dispersion relation for surface gravity waves was used to determine nearshore ocean depth from successive images acquired by the WorldView-2 satellite of the coastal area near Camp Pendleton, California.

Principal component transforms were performed on co-registered images and principal component four was found to very effectively highlight wave crests in the surf zone. Change detection images, which included principal component four from successive images, contained both spatial and temporal information. From these change detection images, wave celerity could be determined and depth inversion could be performed.

For waves farther from shore, principal component four no longer highlighted wave crests. Waves could be resolved within a single RGB composite image with equalization enhancement. The wavelength of a wave above a known depth was measured and the wave period method was used to determine depth for other waves in the propagation direction of this wave. Our depth calculations compared favorably to our reference bathymetry. The spatial resolution for this method of determining depth is higher and perhaps more accurate than our reference bathymetry, particularly in the surf zone.

THIS PAGE INTENTIONALLY LEFT BLANK

## TABLE OF CONTENTS

I. INTRODUCTION .....	1
A. PURPOSE OF RESEARCH .....	1
B. SPECIFIC OBJECTIVES .....	2
II. BACKGROUND .....	3
A. LINEAR FINITE DEPTH DISPERSION RELATION FOR SURFACE GRAVITY WAVES .....	3
B. HISTORY OF REMOTE SENSING DETERMINATION OF WATER DEPTH .....	4
1. Early Investigations .....	4
a. <i>The Waterline Method</i> .....	4
b. <i>The Transparency Method</i> .....	5
c. <i>The Wave Period Method</i> .....	5
d. <i>The Wave Velocity Method</i> .....	6
2. Modern Studies .....	7
III. EXPERIMENTAL APPROACH .....	21
A. PROBLEM DEFINITION .....	21
B. MATERIALS .....	21
1. WorldView-2 Sensor .....	21
2. The Environment for Visualizing Images 4.7 (ENVI) .....	23
C. METHODS .....	24
1. Image Registration .....	24
2. Principal Components Transform .....	24
3. Change Detection .....	24
IV. OBSERVATIONS .....	25
A. WORLDVIEW-2 IMAGERY OF CAMP PENDLETON .....	25
B. WORLDVIEW-2 COLLECTION SIMULATION .....	34
V. ANALYSIS .....	35
A. BATHYMETRY FROM IMAGERY .....	35
B. COMPARISON TO REFERENCE BATHYMETRY .....	44
VI. SUMMARY .....	49
VII. CONCLUSIONS AND FUTURE WORK .....	51
LIST OF REFERENCES .....	53
INITIAL DISTRIBUTION LIST .....	55

THIS PAGE INTENTIONALLY LEFT BLANK

## LIST OF FIGURES

Figure 1.	Sonar bathymetry determination method (From [Gao, 2009, modified from Tripathi & Rao, 2002]) .....	1
Figure 2.	Curves relating wave period to depth and wavelength (From [Williams, 1947]).....	5
Figure 3.	Curves relating water depth to wavelength and celerity (From [Williams, 1947]).....	6
Figure 4.	Plot of error functions $f(kh)$ and $g(kh)$ versus $kh$ (From [Dalrymple et al., 1998]).....	8
Figure 5.	Plot of wave celerity from X-Band marine radar (From [Bell, 1999]) .....	9
Figure 6.	Plot of water depth calculated from X-Band radar data (From [Bell, 1999]) .....	10
Figure 7.	Bathymetry using IKONOS imagery (left) (color scale is red-blue=0-22m depth) and corresponding USGS topographical map (right) (From [Abileah, 2006]).....	11
Figure 8.	Plot of amplitude, phase, cross-shore wave number, and depth calculated from video data (From [Stockdon & Holman, 2000]) .....	12
Figure 9.	Plot of predicted versus measured depth for multiple experiments (From [Holland, 2001]).....	13
Figure 10.	Airborne nearshore area collection geometry a) perspective view b) overhead view (From [Dugan et al., 2001]).....	15
Figure 11.	Example video data showing a) intensity timestack and b) pixel intensity time series (from [Catalan & Haller, 2008]).....	16
Figure 12.	Depth inversion algorithm flowchart (From [Catalan & Haller, 2008]) .....	19
Figure 13.	WorldView-2 Satellite (From [DigitalGlobe, 2009]).....	22
Figure 14.	Comparison of DigitalGlobe satellite spectral coverage (From [DigitalGlobe, 2010b]).....	22
Figure 15.	DigitalGlobe ortho-ready standard 2A image format (From [DigitalGlobe, 2010a]) .....	25
Figure 16.	Google Earth representation of WorldView-2 image data for Camp Pendleton area.....	26
Figure 17.	Image to image registration example performed with a few ground reference points along shoreline .....	27
Figure 18.	Original spectral bands one through eight example .....	28
Figure 19.	Principal component bands one through eight example.....	29
Figure 20.	Principal component four inverse image with transect perpendicular to shore and profile .....	29
Figure 21.	Change from first to second image where wave moves from blue to yellow toward the shore.....	31
Figure 22.	Illustration of Camp Pendleton scene components using multispectral data. Components of the scene highlighted include from left to right; waves, kelp (red), an airplane condensation trail, outflowing river sediment, and the shoreline (white) .....	32

Figure 23.	Illustration of Camp Pendleton scene components using multispectral and panchromatic data .....	33
Figure 24.	Satellite Toolkit simulation of WorldView-2 Camp Pendleton area collection..	34
Figure 25.	Covariance for the spectral bands of the first image .....	36
Figure 26.	Correlation for the spectral bands of the first image .....	36
Figure 27.	Eigenvector representation of principal component bands one through four with PC Band 4 highlighted.....	37
Figure 28.	Eigenvector representation of principal component bands five through eight....	38
Figure 29.	First image to second image change detection .....	39
Figure 30.	Second image to third image change detection .....	39
Figure 31.	First to second to third image change detection showing only additive color mixed wave lines.....	40
Figure 32.	Overlay of surveyed bathymetry to depth measured change detection image ....	41
Figure 33.	Curves relating wave period to depth and wavelength (wavelength units in meters).....	42
Figure 34.	Deeper water waves resolved using 765 bands in RGB triplet representation....	43
Figure 35.	Tide height for March 24, 2010 at closest station to Camp Pendleton (From [National Oceanic and Atmospheric Administration, 2010, August 25]) .....	44
Figure 36.	Bathymetric contours with perpendicular drawn to shoreline overlaid on top of change detection image .....	45
Figure 37.	Nearshore depth profile with data points from wave velocity and wave period methods.....	46
Figure 38.	Nearshore depth profile with error bars (plus 42% for wave velocity, and plus/minus 15% for wave period) .....	48



## LIST OF TABLES

Table 1.	Experimentally derived errors for 10 different wave celerity models (From [Catalan & Haller, 2008]) .....	17
Table 2.	Experimental error estimates of linear and KD86 models (From [Catalan & Haller, 2008]) .....	18
Table 3.	WorldView-2 Specifications (From [DigitalGlobe, 2009]) .....	23
Table 4.	Multispectral image directories showing time between images .....	27
Table 5.	Statistics of the first image computed during principal components transformation .....	35

THIS PAGE INTENTIONALLY LEFT BLANK

## **ACKNOWLEDGMENTS**

I would like to thank the farsighted executives at The Boeing Company who sent me to NPS in order to further develop my technical capabilities. Their faith in me is already paying off. I would like to acknowledge Dr. Olsen for his enthusiasm on this subject which helped to sustain my interest in performing this work. Thanks to Dr. Kruse for his careful critique. Thanks also to Heather for listening when I only wanted to talk about the dispersion relation, and multispectral imagery.

THIS PAGE INTENTIONALLY LEFT BLANK

# I. INTRODUCTION

## A. PURPOSE OF RESEARCH

Wave and tidal processes, and severe storms, can dramatically change nearshore bathymetry over a short time period. Nearshore bathymetry can be accurately collected from a boat using sonar, except in denied waters where these types of measurements would not be allowed. Figure 1 gives an illustration of the sonar bathymetry determination method (Gao, 2009):

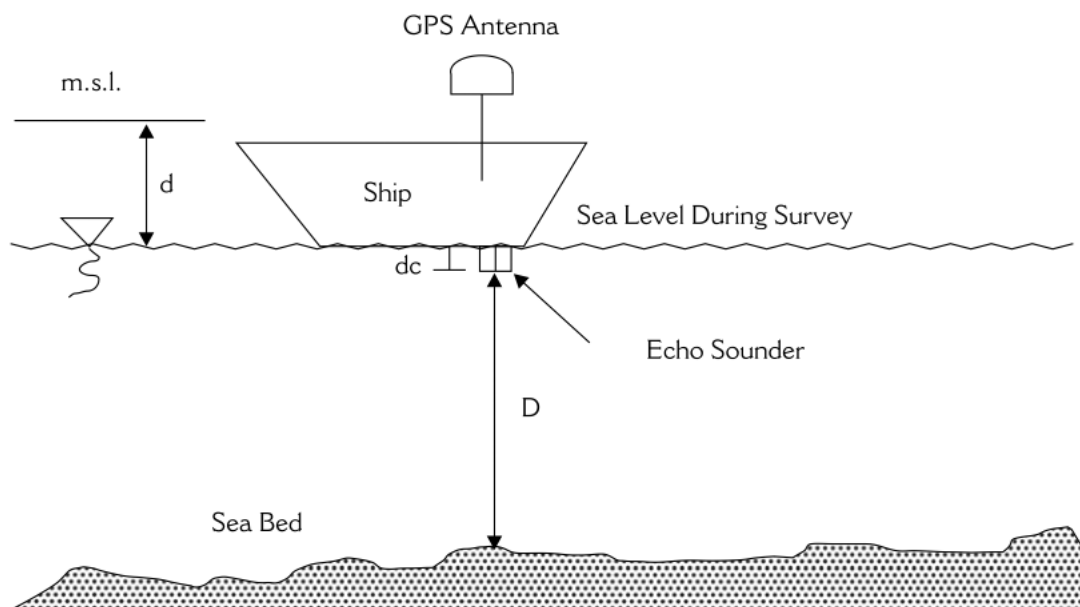


Figure 1. Sonar bathymetry determination method (From [Gao, 2009, modified from Tripathi & Rao, 2002])

Due to the changeable nature of the nearshore bathymetry, the usefulness of a sonar survey would be temporary. Remote sensing measurements from the air may not be feasible since the aircraft could be in danger of being shot down prior to acquiring data over denied territory. Remote sensing from Low Earth Orbit (LEO) can be used over denied territory since the platform is safely out of the range of most weapons systems.

A space-based electro-optical payload will need to have sufficient resolution ( $\sim 2\text{m}$ ) and the ability to take multiple images of the same coastal location in short

succession (6 to 12 s) in order for the bathymetry to be extracted. This research focuses on estimating water depth in nearshore environments using WorldView-2 multispectral images taken in rapid succession. By comparing the same wave in multiple images and knowing the exact time of image acquisition, water depth can be estimated using the linear dispersion relation for surface gravity waves.

## **B. SPECIFIC OBJECTIVES**

The objective of this study was to test the potential of determining nearshore bathymetry using multiple images of a coastal area taken in rapid succession. Being able to determine bathymetry in this manner allows for acquiring knowledge of denied area nearshore bathymetry from a few quick images from a LEO spacecraft. Specifically, this work:

- 1) Uses multiple WorldView-2 multispectral images (which have been registered to each other) taken in rapid succession of the coastal area near Camp Pendleton, California to identify nearshore waves
- 2) Uses image processing techniques in the Environment for Visualizing Images (ENVI) software to enhance wave position and measure wavelengths
- 3) Calculates depth and compiles a list of depth data points
- 4) Compares depth data to reference bathymetric contour data in order to determine accuracy of estimates

The motivation for this work comes from a desire to use modern remote sensing techniques to determine depths without using water transparency methods. Water transparency methods suffer from absorption, reflection, and scattering from choppy seas and from occlusions caused by suspended particulates, marine plant life, and dark bottom sediments (Williams, 1947). The approach used here relies only on being able to resolve the top of the water waves and uses a well-known and simple relationship between wave celerity and depth. Being able to determine water depth in this manner has application to military operations, as well as disaster relief, and humanitarian aid efforts.

## II. BACKGROUND

### A. LINEAR FINITE DEPTH DISPERSION RELATION FOR SURFACE GRAVITY WAVES

The speed of shallow water waves is independent of wavelength ( $\lambda$ ) or wave period (T) and is controlled by the depth of water (Knauss, 1996). Waves travel faster in deeper water. The speed of deep water waves is independent of depth and is determined by  $\lambda$  and T (Knauss, 1996).

Equation 1 shows the relationship between celerity (surface wave phase speed), wavelength, and water depth:

$$c^2 = \frac{g}{k} \tanh(kh) \quad (1)$$

Where  $c$  is the wave celerity,  $g$  is the gravitational acceleration constant,  $k$  is the wave number ( $k = 2\pi/\lambda$ ), and  $h$  is the water depth. This equation is known as the linear finite depth dispersion relation for surface gravity waves. There are approximations that can be used for this relation that depend on water depth and wavelength (Knauss, 1996). These approximations are;

$$\text{when } kh < 0.33, \tanh(kh) \cong kh \quad (2)$$

$$\text{and when } kh > 1.50, \tanh(kh) \cong 1 \quad (3)$$

These approximations yield dispersion relation equations specific for shallow water waves and deep water waves. Equation 4 shows the equation for shallow water waves where water depth is dependent on wave celerity. Equation 5 shows the equation for deep water waves where wave celerity is dependent on wavelength.

$$c_s^2 = gh \quad (4)$$

$$c_d^2 = \frac{g}{k} \quad (5)$$

For intermediate wavelengths, Equation 1 must be used. These equations show that the wave period ( $T = \lambda/c$ ) remains constant from deep water to shallow water, but wave celerity and wavelength decrease proportionally. Wave height (H) also changes from deep water to shallow water, and will further complicate the dispersion relation (Knauss, 1996).

## **B. HISTORY OF REMOTE SENSING DETERMINATION OF WATER DEPTH**

### **1. Early Investigations**

The Normandy invasion by allied forces in World War II presented many logistical challenges including how to land hundreds of boats on beaches controlled by enemy troops (Williams, 1947). Since nearshore coastal areas are dynamic and can change over relatively short periods of time, even previously surveyed bathymetry may not be good enough to ensure the success of military operations where lives may be at risk. In W.W. Williams' seminal paper from 1947, he outlines four ways of attempting to accurately determine bathymetry remotely;

#### ***a. The Waterline Method***

Using images of shorelines taken at different times, contours of the waterlines are drawn. The highest contour will correspond to high tide, while the lowest contour will correspond to low tide. In ideal conditions, this method will only be able to produce bathymetric contours for the difference between high and low tides, which may only correspond to a few feet. Uncertainty using this method includes; image scaling and rectification, accurately mapping contours to tide height from tables, false waterlines due to the breaking waves flowing up on the beach, and problems resolving the actual waterline in the images (Williams, 1947).

The waterline method was used extensively during World War II and was also used during World War I to determine beach gradients on the coast of Flanders (Williams, 1947). The utility of this method is limited since only very shallow depths can be mapped where tidal processes are present. For any body of water that experiences very limited tides or no tides at all, the waterline method is not useful.



**b. The Transparency Method**

Incident light on the surface of the water will be; reflected, absorbed, transmitted, and scattered by varying amounts (Olsen, 2007). The light that is transmitted will reflect off of light colored sediments and be transmitted up through the water and toward the imaging sensor, in very shallow water. As the water gets deeper, the two-way attenuation of the transmitted light energy prevents the reflected energy from the bottom sediments from escaping the water. When this happens, it is no longer possible to see bottom.

This method suffers from uncertainties associated with; choppy seas (increasing scattering), suspension of particulates in the water (preventing light from transmitting through entire water column), and dark plant and sediment materials (increasing absorption and decreasing reflection of incident light). This method was used to map a section of the Seine river in 1943 (Williams, 1947).

**c. The Wave Period Method**

This method involves studying images of deeper water waves and determining their wavelengths. The distance from shore must be determined in order to reference known bathymetry to determine depth where the wave is located. Figure 2 shows a plot of curves used to determine wave period.

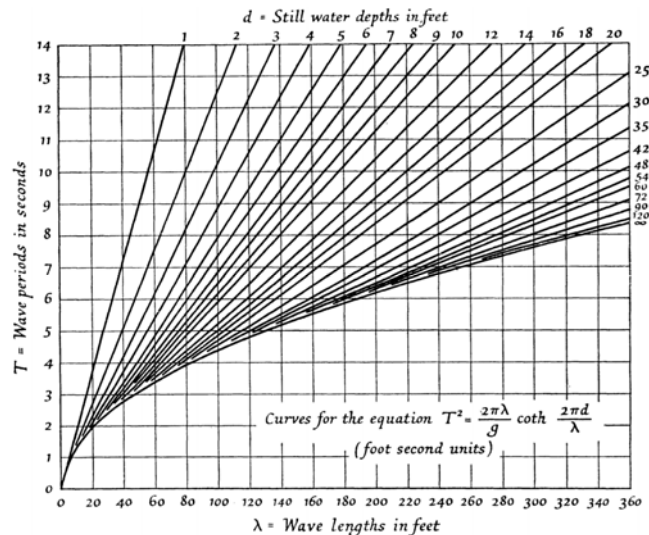


Figure 2. Curves relating wave period to depth and wavelength (From [Williams, 1947])

When wavelength and depth have been established, a plot of mathematically derived curves relating wavelength and depth to period can be referenced in order to determine wave period. Once this wave period has been determined, different wavelength waves that intersect a horizontal line drawn on the plot for the period can be directly related to water depth (Williams, 1947).

The wave period method requires an initial known depth. Small inaccuracies in the resultant period estimates can cause large errors in depth calculation (Williams, 1947). This method also suffers from the difficulty in accurately measuring wavelengths in deeper water where individual waves are not as easily distinguishable (Williams, 1947).

#### *d. The Wave Velocity Method*

The celerity of an ocean wave can be used to determine depth. In order to determine celerity, wavelength must be measured from successive images with a known interval between them. Figure 3 shows a plot of curves used to determine water depth.

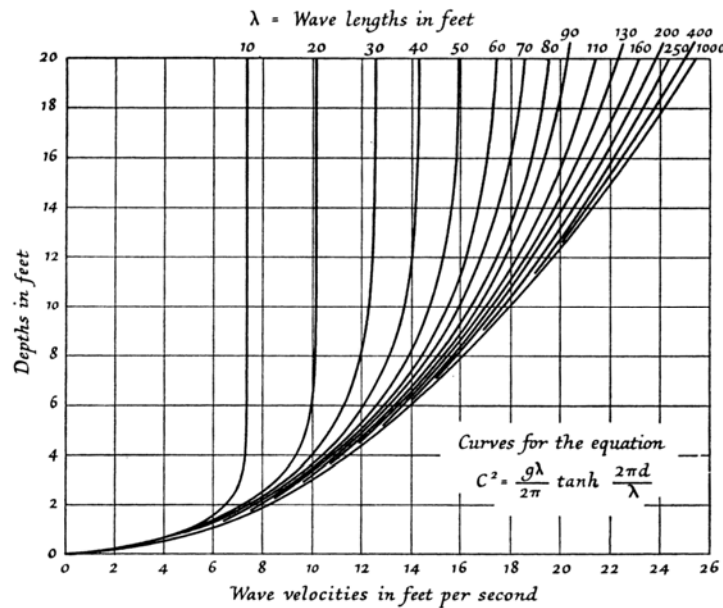


Figure 3. Curves relating water depth to wavelength and celerity (From [Williams, 1947])

Deep water waves travel faster than shallow water waves and have no dependence on water depth. As waves reach depths shorter than their length, they slow down. In shallow water, water depth can be calculated from wave celerity and gravitational acceleration alone (Williams, 1947).

The wave velocity method is useful since depth can be calculated from a simple mathematical expression once celerity is known. In shallow water, waves are well defined with long bright crests and are easier to distinguish in imagery. With multiple images of the same coastal region and a known interval between images, wave celerity can be calculated directly. Cameras with clocks were not always available, which decreased the usefulness of this method (Williams, 1947).

The wave methods described above suffer from uncertainties including; accuracy of image acquisition times, scale and registration of images, complex wave patterns skewing measurements, and low image resolution (Williams, 1947). Modern remote sensing systems and tools can be used to overcome some of these limitations. Remote sensing spacecraft typically have very accurate clocks, and image acquisition times are embedded in image metadata files. Images can be registered to each other using software tools like the Environment for Visualizing Images (ENVI). Commercial imagery from space can provide up to 50cm resolution improving the ability to resolve ocean waves.

## **2. Modern Studies**

Remotely sensed images from space can provide a nearly comprehensive summary of wave processes for relatively large areas of the sea surface (Dalrymple, Kennedy, Kirby, & Chen, 1998). A single image of a coastal area can be used to determine bathymetry through the use of the linear dispersion relation, while the “lagged correlation method” where multiple images taken over a short time period are used together can be more useful (Dalrymple et al., 1998). With a single image, wavelength must be measured and period estimated. Period does not change from deep to shallow water, but it must be estimated for the deep water case. With multiple images, short time samples (~1 s) are needed for deep water depth estimation.

Sequential images of the same target location will show waves of various wave numbers and wave frequencies propagating with characteristic phase speeds. The lag-correlation method uses multiple images to extract the wave number and wave frequency (Dalrymple et al., 1998). These parameters can be used to estimate depth.

The linear dispersion relation can be rearranged to express depth as a function of x and y position (Dalrymple et al., 1998):

$$h(x,y) = \frac{1}{k(x,y)} \tanh^{-1}(\sigma^2 / g) \quad (6)$$

When the derivative of Equation 6 is taken (and h(x,y) is divided out), the error associated with depth can be expressed as a function of the error in wave number (g(kh)) and wave frequency (f(kh)) (Dalrymple et al., 1998):

$$\left(\frac{dh}{h}\right) = 2\left(\frac{\sinh 2kh}{2kh}\right)\left(\frac{d\sigma}{\sigma}\right) - \left(1 + \frac{\sinh 2kh}{2kh}\right)\left(\frac{dk}{k}\right) = f(kh)\left(\frac{d\sigma}{\sigma}\right) - g(kh)\left(\frac{dk}{k}\right) \quad (7)$$

The error terms f(kh) and g(kh) double any error in wavelength determination in shallow water, and increase exponentially with kh (Dalrymple et al., 1998). Figure 4 shows how these error terms increase with increasing depth.

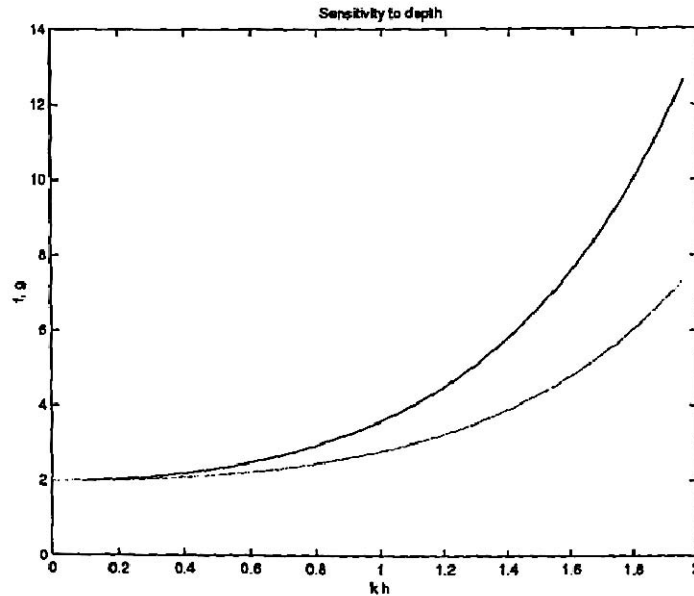


Figure 4. Plot of error functions f(kh) and g(kh) versus kh (From [Dalrymple et al., 1998])

There is more error associated with calculating depth in deep water since wave phase speed has little dependence on depth. For deep water, any error associated with estimations of wave phase speed or wave number will be greatly increased (Dalrymple et al., 1998). Another source of uncertainty comes from wave heights causing depth overestimation.

X-Band marine radar images can also be used to estimate water depth in nearshore areas. A sequence of radar images can be analyzed to map how wave behavior changes in these areas. Wave period must be calculated from the radar data and used to determine water depth (Bell, 1999). Wave celerity and direction can be mapped with the radar. Bathymetric inversion is used once peak wave period has been measured from the radar data. Linear wave theory use for nearshore areas suffers from uncertainties associated with nonlinear processes, but allows for a good approximation of depth (Bell, 1999). Figure 5 shows a plot of wave celerity using an X-Band marine radar system. The water depth plot shown in Figure 6 was calculated using the radar data and the linear wave theory.

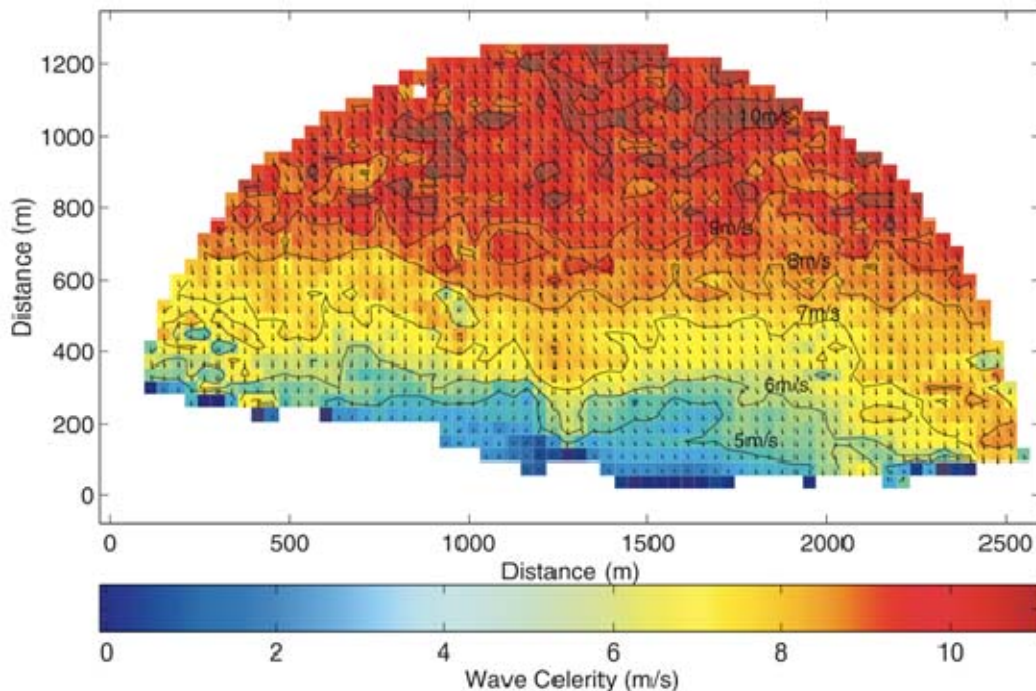


Figure 5. Plot of wave celerity from X-Band marine radar (From [Bell, 1999])

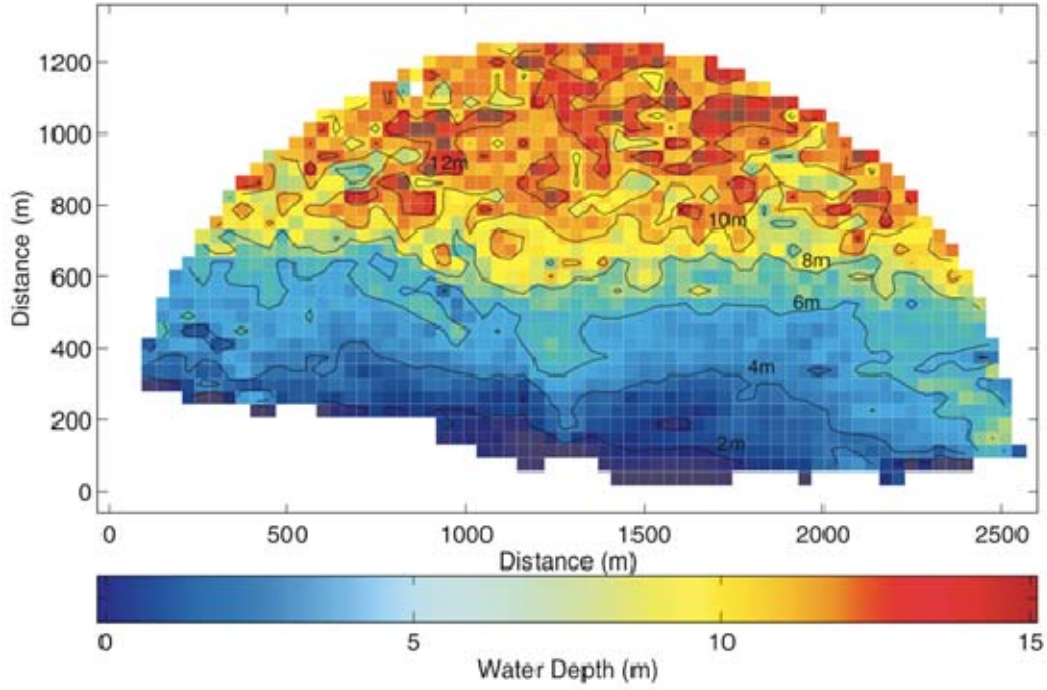


Figure 6. Plot of water depth calculated from X-Band radar data (From [Bell, 1999])

In nearshore areas, the wave period has less influence on wave celerity. Nonlinear wave processes will contribute to larger wave celerities than predicted with the linear dispersion relation (Bell, 1999). This will cause depth estimates to be greater than actual depths. In order to improve this uncertainty, the use of higher order wave theory must be used (Bell, 1999).

One known previous attempt has been made to measure coastal bathymetry using satellite imagery of wave motions (Abileah, 2006). This implementation uses one meter imagery from the IKONOS satellite of the Coronado Island, San Diego area. The Fourier transform is used to convert image intensity into wave number (Abileah, 2006). The wave number spectrum at a time  $t$  is related to the wave number spectrum at time  $t=0$  by the following equation where  $U$  is ocean current:

$$S_t = S_0 e^{-i \left( \sqrt{g|k| \tanh(|k|d)} + [U_x, U_y] \cdot [k_x, k_y] \right)} \quad (8)$$

The phase change between two or more of the image transformations can be used to determine both current and depth. Figure 7 shows an example of how this process can produce depths using the IKONOS data (Abileah, 2006):

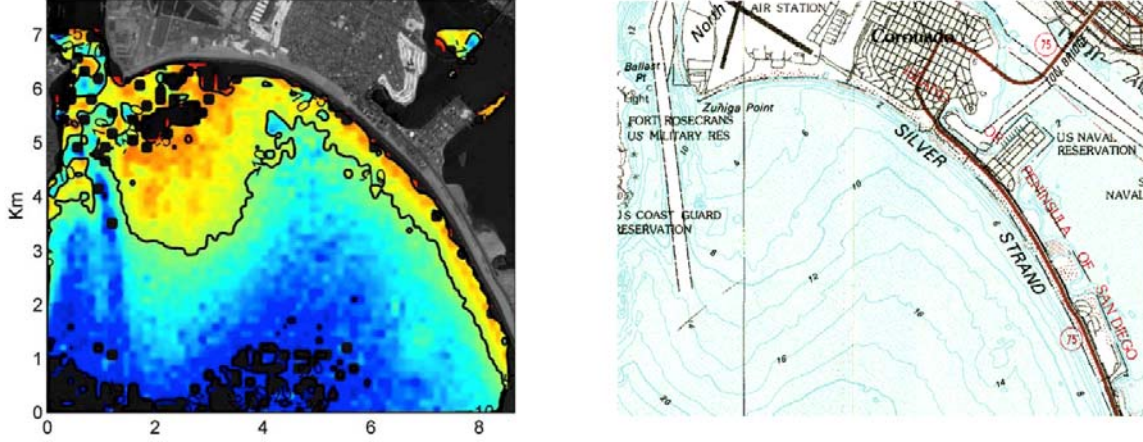


Figure 7. Bathymetry using IKONOS imagery (left) (color scale is red-blue=0-22m depth) and corresponding USGS topographical map (right) (From [Abileah, 2006])

Video image processing can also be used to estimate the depth of nearshore areas. Amplitude and phase are computed from the video imagery and the slope of the phase is used to calculate the cross-shore wave number (Stockdon & Holman, 2000). Depth can then be calculated using a modified depth inversion equation where  $k_x(x)$  is cross-shore wave number,  $k_y(x)$  is long-shore wave number, and  $\sigma^2$  is variance (Stockdon & Holman, 2000):

$$h(x) = \frac{\tanh^{-1} \left( \frac{\sigma^2}{g \sqrt{k_x^2(x)^2 + k_y^2(x)^2}} \right)}{\sqrt{k_x^2(x)^2 + k_y^2(x)^2}} \quad (9)$$

Pixel intensity as a function of position and time is used as the input signal for the video technique. The data is Fourier transformed, normalized by a matrix of variances at each position, and the complex eigenvector of the first mode is used for amplitude and phase calculations (Stockdon & Holman, 2000). Figure 8 shows sample results from this process (Stockdon & Holman, 2000):

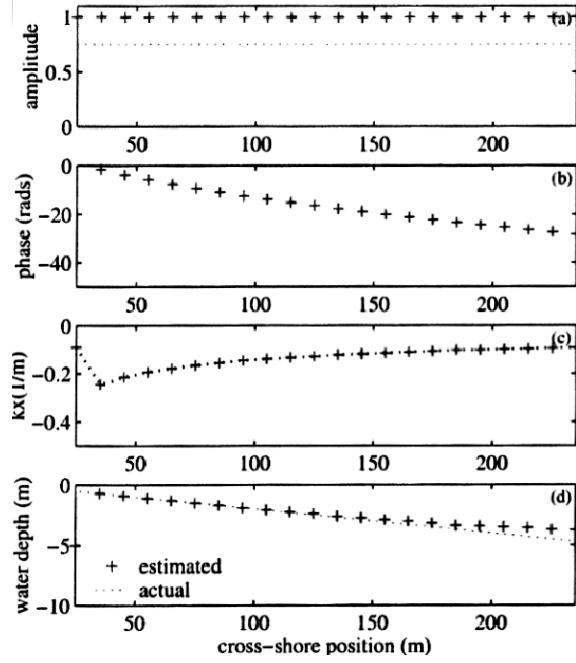


Figure 8. Plot of amplitude, phase, cross-shore wave number, and depth calculated from video data (From [Stockdon & Holman, 2000])

Solitary theory modifies the linear dispersion theory to account for wave heights. If wave heights can be estimated, the celerity of a solitary wave (single wave crest) in shallow water is just (Stockdon & Holman, 2000):

$$c = \sqrt{g(h + H)} \quad (10)$$

The depth uncertainty between using linear theory versus solitary theory can be shown by relating the two equations to one another where  $c_s$  is wave celerity from solitary theory, and  $H$  is wave height where  $H/h$  is assumed to be 0.42 in the surf zone (Stockdon & Holman, 2000):

$$\frac{h_1}{h_2} = \frac{\left(\frac{c^2}{g}\right)}{\left(\frac{c_s^2}{g(1 + H/h)}\right)} = \frac{\left(\frac{c^2}{g}\right)}{\left(\frac{c_s^2}{1.42g}\right)} = 1.42 \quad (11)$$

This equation shows that errors associated with depth calculations using linear theory of up to 42% may be possible. In order to mitigate these errors without including



wave height (which may be difficult to obtain from remotely sensed imagery) in depth calculations, low amplitude waves a little farther away from shore should be used (Stockdon & Holman, 2000).

The linear dispersion relation has been found to very accurately predict water depth for waves outside of the surf zone using extensive field measurements (Holland, 2001). Inside the surf zone, wave height increases celerity. Using linear theory, which does not account for wave height, will underestimate the celerity and result in overestimates for water depth (Holland, 2001). The surf zone of a given location can vary greatly. The surf zone at a site near Duck, NC was found to be where water was less than 4m deep (Holland, 2001). For depth inversion calculations outside the surf zone, errors of 3% to 9% from measured depths were observed. Inside the surf zone, errors over 50% were common (Holland, 2001). Figure 9 shows how errors increased with shallower depths:

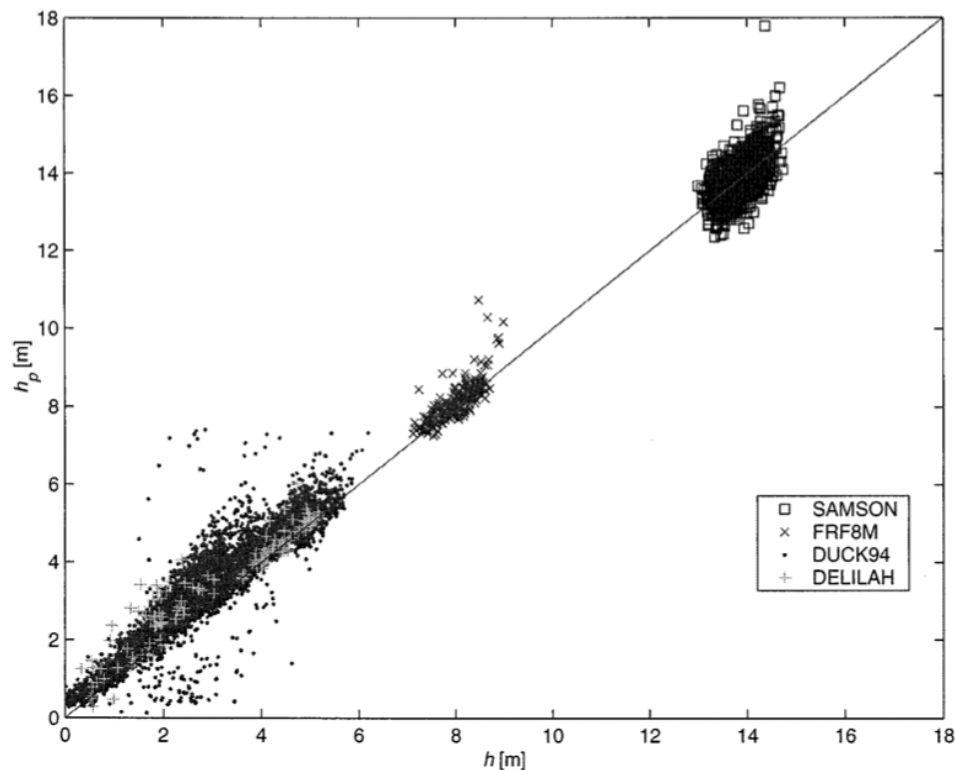


Figure 9. Plot of predicted versus measured depth for multiple experiments (From [Holland, 2001])

Taking wave height into account when performing bathymetric inversion will improve the accuracy of shallow water depth prediction. The problem remains to be able to determine wave height from remote sensing imagery.

If wave heights cannot be determined from remote sensing imagery, they could be estimated in order to reduce uncertainty. The depth of water would be that calculated by linear dispersion theory minus the height of the wave. Concentrating on resolving waves outside of the surf zone allows a solution that neglects wave height, but will have challenges associated with being able to resolve the waves in optical imagery (Holland, 2001).

Studies have been performed with multiple images from airborne platforms to determine nearshore ocean depth (Dugan, Piotrowski, & Williams, 2001). The images were mapped and rectified, and radiance data was Fourier transformed to create frequency-wave number spectra for the modulations caused by ocean waves. This produced spectra with information on the wave characteristics (celerity, wavelengths, etc.) that were used to predict water depth using linear dispersion theory (Dugan et al., 2001).

In order to overcome problems associated with image registration, an inertial navigation system (INS) was mounted on the camera turret in order to provide camera attitude and camera position using the Global Positioning System (GPS) (Dugan et al., 2001). The collection geometry of this airborne platform is shown in Figure 10 (Dugan et al., 2001):

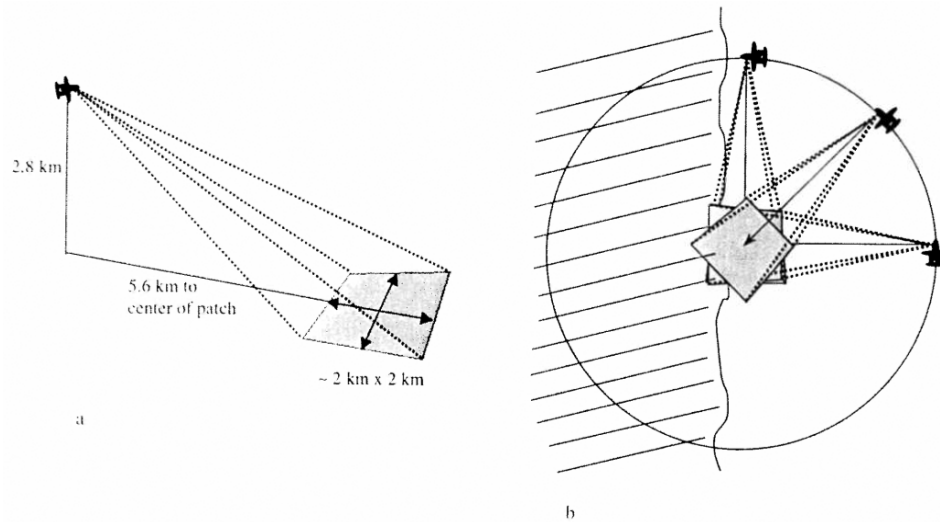


Figure 10. Airborne nearshore area collection geometry a) perspective view b) overhead view (From [Dugan et al., 2001])

The process of producing high resolution frequency-wave number spectra was enabled primarily through the use of large image sub-patches, high quality camera hardware, and accurate mapping techniques. This resulted in depth estimates with errors of 5% to 13% with respect to the surveyed bathymetry (Dugan et al., 2001).

Uncertainty in the depth inversion process can be characterized by; measurement accuracy for wave phase speed and wave height, and choice of depth inversion model for the observed wave conditions (Catalan & Haller, 2008). The complex relationship between wave phase speed and water depth involves nonlinear processes, which can be very difficult to account for with remotely sensed data (Catalan & Haller, 2008). Linear models of wave celerity have been found to underestimate phase speed since some of the wave energy is going into the  $z$  direction (wave crest and trough) (Catalan & Haller, 2008). The two main things that affect phase speed estimation are; amplitude dispersion, which accounts for nonzero wave amplitudes, and frequency dispersion, which accounts for the relative depth of water (Catalan & Haller, 2008).

Large scale laboratory experiments have been performed using high resolution remote sensing video data, and surface elevation data from in-situ wave gauges in order

to compare the accuracy of wave celerity models in nearshore areas (Catalan & Haller, 2008). Figure 11 shows example video data from these experiments:

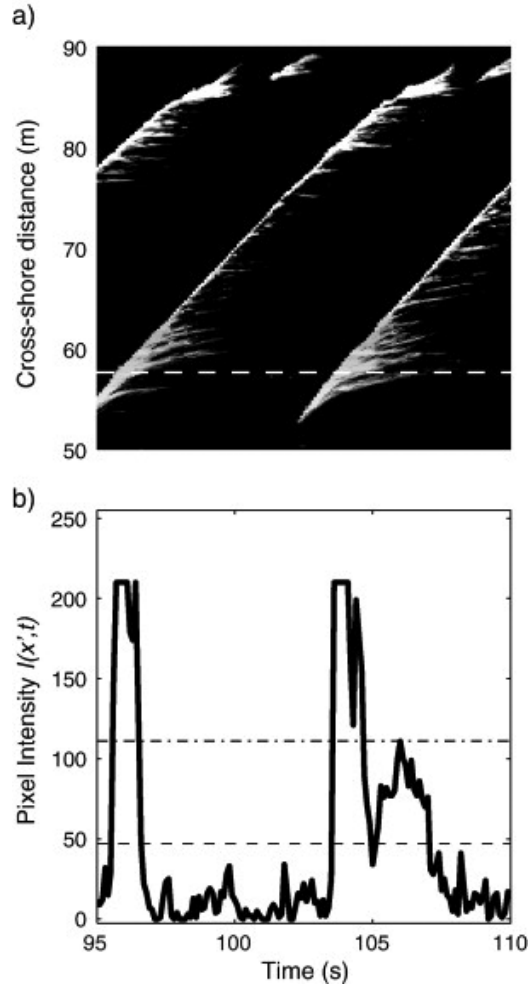


Figure 11. Example video data showing a) intensity timestack and b) pixel intensity time series (from [Catalan & Haller, 2008])

The surf zone was chosen for comparison since in this area, nonlinearities are known to add uncertainty in the depth inversion method of extracting bathymetry. Results for this experiment are shown in Table 1 where  $\bar{R}^c$  is the mean relative error and  $\bar{R}_{RMS}^c$  is the average root-mean-square error for each model (Catalan & Haller, 2008).

Table 1. Experimentally derived errors for 10 different wave celerity models (From [Catalan & Haller, 2008])

Model	Equation	$\bar{R}^c$	$\bar{R}_{RMS}^c$
Linear theory	$c^2 = \frac{g}{k} \tanh(kh)$	-7.4	10.5
Solitary	$c = \sqrt{gh \left(1 + \frac{H}{h}\right)}$	17.9	19.2
Modified shallow	$c = 1.3\sqrt{gh}$	24.0	25.7
Cnoidal theory	$c = \sqrt{gh \left[1 + \frac{H}{mh} \left(2 - m - 3\frac{E}{K}\right)\right]}$	7.0	9.1
Modified cnoidal	$c = \sqrt{gh(1 + f(m)H^*/h)}$		
	$H^* = H_{local}$	5.0	10.1
	$H^* = H_{max}$	13.3	14.7
	$H^* = H_{off}$	9.1	11.9
Bore	$c_b^2 = gh \frac{d_t d_b}{h^3} \frac{(d_t + d_b)}{2}$	13.3	14.7
Shock	$c = -2\sqrt{gh_m} + 2\sqrt{gh_t} + \sqrt{\left(g \frac{h_t}{h_t} \left(\frac{h_t + h_b}{2}\right)\right)}$	24.1	25.1
KD86	$c^2 = g/k(1 + f_1 \epsilon^2 D) \tanh(kh + f_2 \epsilon)$	2.8	8.0
Hedges	$c^2 = \frac{g}{k} \tanh(k(h + H))$	11.1	12.7
Booij	$c^2 = \frac{g}{k} \tanh(k(h + H/2))$	2.7	8.0

Several of the nonlinear models from the academic literature (KD86 (Kirby & Dalrymple, 1986) and Booij in particular) perform better than the linear models in the surf zone (Catalan & Haller, 2008). The standard linear dispersion relation for surface gravity waves or “Linear theory” is shown to underestimate phase speed by not taking wave height into account. The “Modified shallow” model, which is a version of the “Solitary” model where the relation  $H/h$  is taken to be a constant of 0.42, is shown to greatly overestimate the wave phase speed. All of the models used, except for “Linear theory” and “Modified shallow,” require a known wave height or local water depths under wave crest and trough in order to obtain more accurate results (Catalan & Haller, 2008). The determination of wave heights is especially difficult to derive from remote sensing imagery because the relative height of the waves is very small with respect to the platform to target range.

The linear theory can be compared to KD86 (the most complex celerity equation) in terms of how accurately they can determine depth. Table 2 shows experimental data of

depth inversion using each model where a positive percent error corresponds to an overprediction of depth, D refers to difference errors and R relative errors for multiple cases (Catalan & Haller, 2008):

Table 2. Experimental error estimates of linear and KD86 models (From [Catalan & Haller, 2008])

Case	Linear				KD86			
	$\bar{D}$	$D_{rms}$	$\bar{R}$	$R_{rms}$	$\bar{D}$	$D_{rms}$	$\bar{R}$	$R_{rms}$
	m	m	%	%	m	m	%	%
35	0.05	0.10	9.41	19.26	-0.10	0.14	-13.13	20.47
36	0.05	0.11	5.28	14.36	-0.12	0.16	-20.29	27.20
37	0.25	0.26	41.10	44.83	0.08	0.11	14.75	19.85
38	0.23	0.25	39.02	44.89	0.05	0.11	10.93	20.55
39	0.15	0.18	27.15	33.30	-0.03	0.11	-1.39	15.16
Median	0.17	0.18	28.20	31.65	-0.01	0.05	0.94	9.70

Table 2 shows experimentally that the KD86 model can be more accurate on average at predicting depth in the surf zone. The greater accuracy comes at the price of complexity and the need for knowing the wave heights. The full KD86 model is described by the following equations (Catalan & Haller, 2008):

$$c^2 = g/k(1 + f_1 \varepsilon^2 D) \tanh(kh + f_2 \varepsilon) \quad (12)$$

where  $\varepsilon = kH/2$  and H is the wave height and:

$$D = \frac{8 + \cosh 4kh - 2 \tanh^2 kh}{8 \sinh^4 kh} \quad (13)$$

$$f_1(kh) = \tanh^5(kh) \quad (14)$$

$$f_2(kh) = \left( \frac{kh}{\sinh(kh)} \right)^4 \quad (15)$$

If wave heights are known, a wave celerity model that incorporates this factor can be used in the depth inversion process for determining water depth. In all other cases, a

linear model must be used. Figure 12 shows a flowchart for the depth inversion algorithm where dashed lines are the steps for linear inversions and solid lines are the extra steps required for nonlinear inversions (Catalan & Haller, 2008):

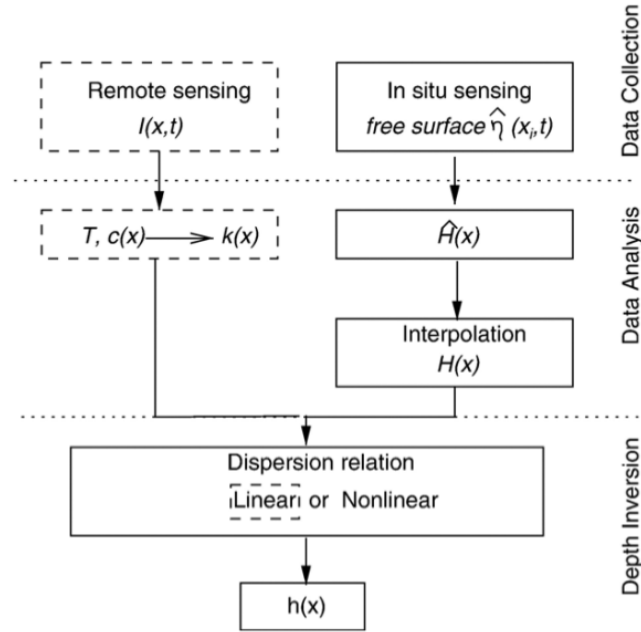


Figure 12. Depth inversion algorithm flowchart (From [Catalan & Haller, 2008])

THIS PAGE INTENTIONALLY LEFT BLANK



### **III. EXPERIMENTAL APPROACH**

#### **A. PROBLEM DEFINITION**

Depth inversion using space based imagery is a convenient method to measure the bathymetry of nearshore areas in remote or denied locations. This method has advantages over the transparency method, which suffers from absorption, reflection and scattering (Olsen, 2007) off of suspended particulate matter, aquatic plants, and dark bottom sediments (Williams, 1947). Depth inversion requires that there are visible waves in the data, and that their wavelengths and celerities can be determined.

This study uses multispectral imagery acquired by the WorldView-2 spacecraft of the coastal area near Camp Pendleton, California to see if it offers advantages for determining nearshore depth using the linear finite depth dispersion relation for surface gravity waves. Commercial imaging spacecraft can provide up to 50 cm resolution panchromatic imagery, but this is excessively high when used for resolving things as large as ocean waves. Because increased spatial resolution will not improve the ability to perform linear depth inversion, we will determine if the increased spectral resolution provided by WorldView-2 can provide a benefit for this method.

#### **B. MATERIALS**

##### **1. WorldView-2 Sensor**

WorldView-2 is the third satellite in DigitalGlobe's commercial satellite constellation (Figure 13). It was built by Ball Aerospace & Technologies Corp. and launched in October 2009.

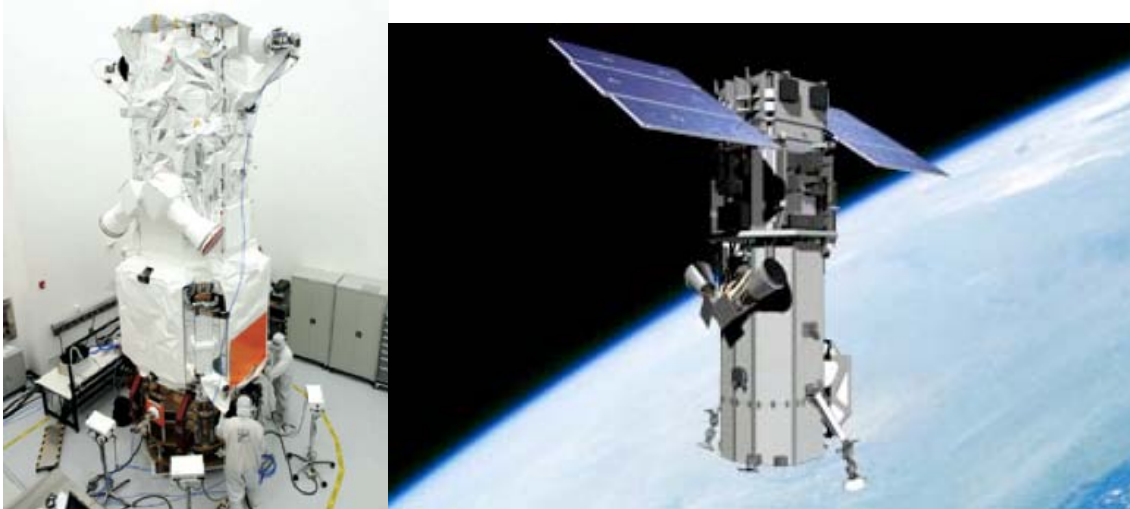


Figure 13. WorldView-2 Satellite (From [DigitalGlobe, 2009])

WorldView-2 is the first commercial satellite to combine both high resolution panchromatic and 8-band multispectral sensor capabilities and is a significant spectral performance improvement over DigitalGlobe's two previous satellites QuickBird and WorldView-1 (Figure 14). The panchromatic sensor is capable of 46 cm resolution at nadir. The multispectral sensors are capable of 1.84 m resolution at nadir (DigitalGlobe, 2009).

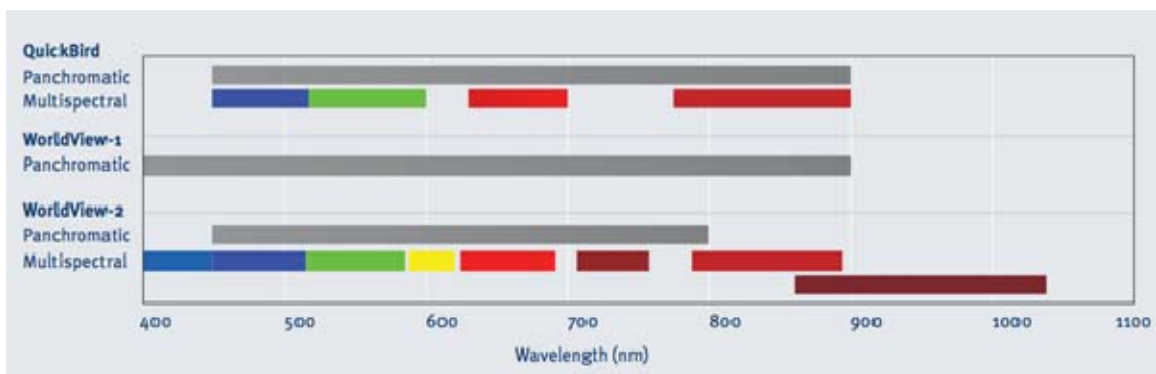


Figure 14. Comparison of DigitalGlobe satellite spectral coverage (From (DigitalGlobe, 2010b))

Table 3 shows important specifications of the WorldView-2 spacecraft and payload:

Table 3. WorldView-2 Specifications (From [DigitalGlobe, 2009])

<b>Launch Information</b>	Date: October 8, 2009 Launch Vehicle: Delta 7920 (9 strap-ons) Launch Site: Vandenberg Air Force Base, California
<b>Orbit</b>	Altitude: 770 kilometers Type: Sun synchronous, 10:30 am descending node Period: 100 minutes
<b>Mission Life</b>	7.25 years, including all consumables and degradables (e.g. propellant)
<b>Spacecraft Size, Mass and Power</b>	4.3 meters (14 feet) tall x 2.5 meters (8 feet) across 7.1 meters (23 feet) across the deployed solar arrays 2800 kilograms (6200 pounds) 3.2 kW solar array, 100 Ahr battery
<b>Sensor Bands</b>	Panchromatic: 450 - 800 nm 8 Multispectral: Coastal: 400 - 450 nm      Red: 630 - 690 nm Blue: 450 - 510 nm      Red Edge: 705 - 745 nm Green: 510 - 580 nm      Near-IR1: 770 - 895 nm Yellow: 585 - 625 nm      Near-IR2: 860 - 1040 nm
<b>Sensor Resolution</b>	Panchromatic: 0.46 meters GSD at nadir*, 0.52 meters GSD at 20° off-nadir Multispectral: 1.84 meters GSD at nadir*, 2.08 meters GSD at 20° off-nadir
<b>Dynamic Range</b>	11-bits per pixel
<b>Swath Width</b>	16.4 kilometers at nadir

WorldView-2 is also capable of collecting multiple point targets that are 16.4 km x 16.4 km in size. Multiple images of the same point target can be collected in rapid succession due to the increased agility of this spacecraft (acceleration=1.5 deg/s/s, rate=3.5 deg/s) (DigitalGlobe, 2009).

## 2. The Environment for Visualizing Images 4.7 (ENVI)

The Environment for Visualizing Images version 4.7 was used to manipulate WorldView-2 imagery of nearshore waves. ENVI 4.7 is a powerful tool used for image processing for remote sensing applications (ITT Visual Information Solutions, 2010). It is capable of performing image to image registration. Image features can be accurately measured using the built-in measurement tool. Principal components transformations can be performed on images for decorrelation of variables. A form of change detection can be performed on co-registered images by representing different images as different colors in an RGB triple representation of the data.

## **C. METHODS**

### **1. Image Registration**

The WorldView-2 imagery provided by DigitalGlobe of the coastal area near Camp Pendleton are ortho-ready standard 2A format and are in geographic latitude/longitude coordinates. In this format, the image is projected onto a reference ellipsoid without the rough terrain model applied. A constant base elevation is used instead (DigitalGlobe, 2010a). Image to image registration using ground reference points can be performed on these images using the ENVI map registration function. Images of the Camp Pendleton area were co-registered using the resampling, scaling and translation (RST) method with nearest neighbor resampling for ocean wave comparison purposes.

### **2. Principal Components Transform**

Using principal components analysis, a number of potentially correlated variables can be linearly transformed into a smaller set of uncorrelated variables (Jackson, 2003). The increased degrees of freedom offered by the eight band multispectral image data can be examined using image processing techniques. Principal components transforms were performed and statistics computed on the multispectral images using the ENVI principal components transform function in order to determine whether these could aid in wave detection.

### **3. Change Detection**

The WorldView-2 image data consist of multiple time spaced images of the same coastal scene. Co-registered images can be placed in each band of an RGB triple image representation to show how things change from image to image. For comparing two images, the second image is placed in the red and green bands while the first image is placed in the blue band. Multiple images were compared in this way to show the wave moving from blue to yellow (red combined with green) from one image to the next image.

## IV. OBSERVATIONS

### A. WORLDVIEW-2 IMAGERY OF CAMP PENDLETON

The WorldView-2 imagery of the coastal area near Camp Pendleton, California provided by DigitalGlobe consists of ten panchromatic and multispectral images taken in rapid succession during a single pass of the spacecraft over the area on March 24, 2010. The images are in ortho-ready standard 2A format and are in geographic latitude/longitude coordinates. Figure 15 shows how the images are broken up into two parts each and designated at row 1 column 1 (R1C1) and row 2 column 1 (R2C1).

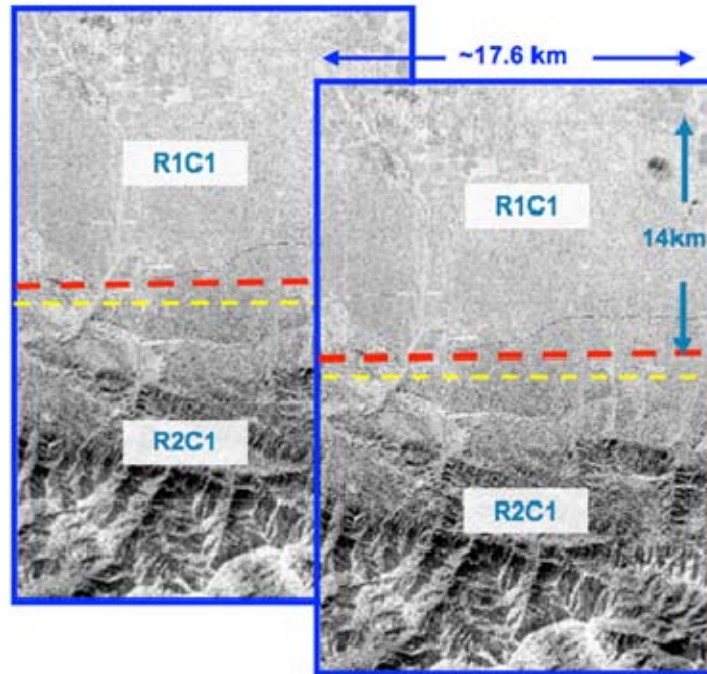


Figure 15. DigitalGlobe ortho-ready standard 2A image format (From [DigitalGlobe, 2010a])

The Camp Pendleton area scene consists of about half ocean and half land. This improves the ability to co-register the images while providing a wide field of view of the ocean to find different types of waves. Figure 16 shows the layout of the Camp Pendleton scene with both row 1 and row 2 in a Google Earth representation of the first collected image.

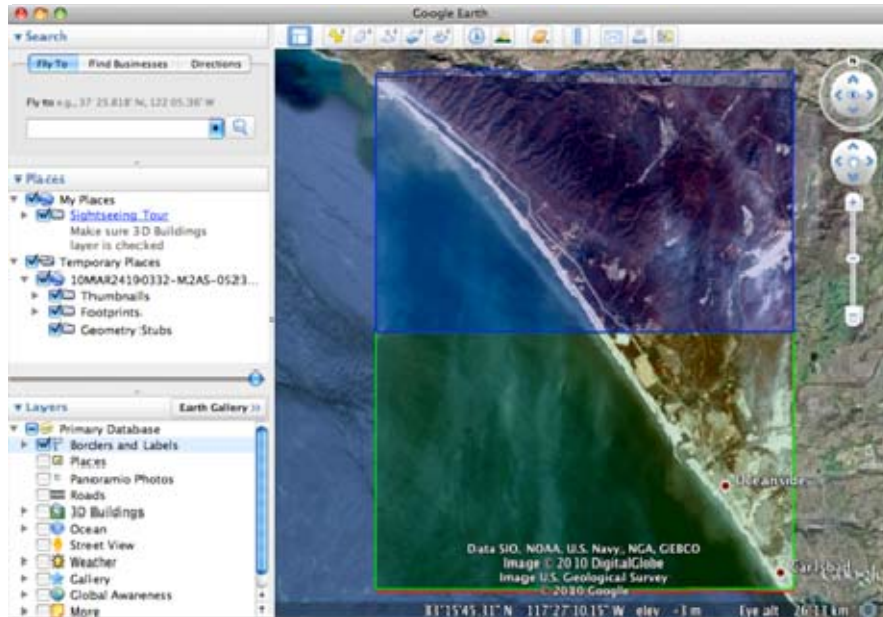


Figure 16. Google Earth representation of WorldView-2 image data for Camp Pendleton area

Image metadata for the ten multispectral images were examined for information on image acquisition times. The “first line time” corresponds to exposure of the first line in the image. The time delta between images is shown in Table 4. The time between successive images varies from 10.40 seconds to 11.00 seconds. The time delta between the first and second image, second and third image, and third and fourth image is the same to a hundredth of a second. The times given in Table 4 are Zulu time. Pacific daylight savings time began on March 14 in 2010, so 1900 corresponds to noon PDT. Note that the image (folder) names are arbitrary, and derive from the vendor’s processing string.

Table 4. Multispectral image directories showing time between images

WorldView-2 Data: March 24, 2010						
Directory Name: 052365928020_01						
Folder Name	Mean GSD X	Mean GSD Y	Mean Sat AZ	Mean Sat EL	First Line Time	Delta Time
P002_MUL	2.087	2.374	277.8	61.2	19:03:31.83	0
P007_MUL	2.102	2.425	267.1	60.1	19:03:42.63	10.80
P009_MUL	2.149	2.503	257.6	58.2	19:03:53.43	10.80
P006_MUL	2.229	2.609	249.5	55.8	19:04:04.23	10.80
P008_MUL	2.337	2.741	242.9	53.1	19:04:14.83	10.60
P004_MUL	2.481	2.910	237.3	50.1	19:04:25.83	11.00
P010_MUL	2.647	3.107	232.9	47.2	19:04:36.43	10.60
P005_MUL	2.841	3.338	229.2	44.4	19:04:47.03	10.60
P003_MUL	3.057	3.603	226.2	41.6	19:04:57.43	10.40
P001_MUL	3.299	3.908	223.6	39.1	19:05:07.83	10.40

The images can all be registered to either image eight or image four which are the middle two images. The first three images were registered to image eight using four ground reference points located near the water line. The first ground reference point was chosen near the upper left corner of the image, the second was chosen near the bottom of the image, and the third and fourth were chosen near the center of the coastline in the image. Figure 17 shows an example image with the ground control points. A limited set of control points was purposely chosen because the focus was on the flat ocean surface. It is difficult to estimate the registration error for the open water, given the lack of control points in the water. Typical errors for this type of registration are a few pixels.

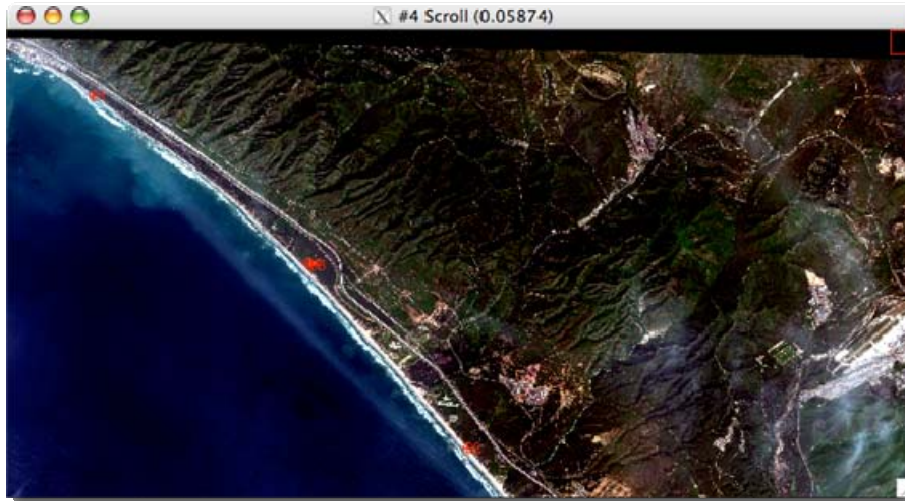


Figure 17. Image to image registration example performed with a few ground reference points along shoreline



After each of the first three images were co-registered to image eight, principal component transforms were performed on each image. The WorldView-2 multispectral images consist of eight distinct spectral bands; Coastal Blue, Blue, Green, Yellow, Red, Red-Edge, NIR1, and NIR2 (DigitalGlobe, 2010b). Eight band multispectral images provide increased degrees of freedom when performing principal component transforms of the data. Figure 18 shows each of the eight original spectral bands for the first image of an area with many visible waves. Figure 19 shows each of the eight principal component bands for the first image. Principal component four highlights the waves with distinct narrow lines at the wave crests without the additional detail and washed out features shown in the other principal components.

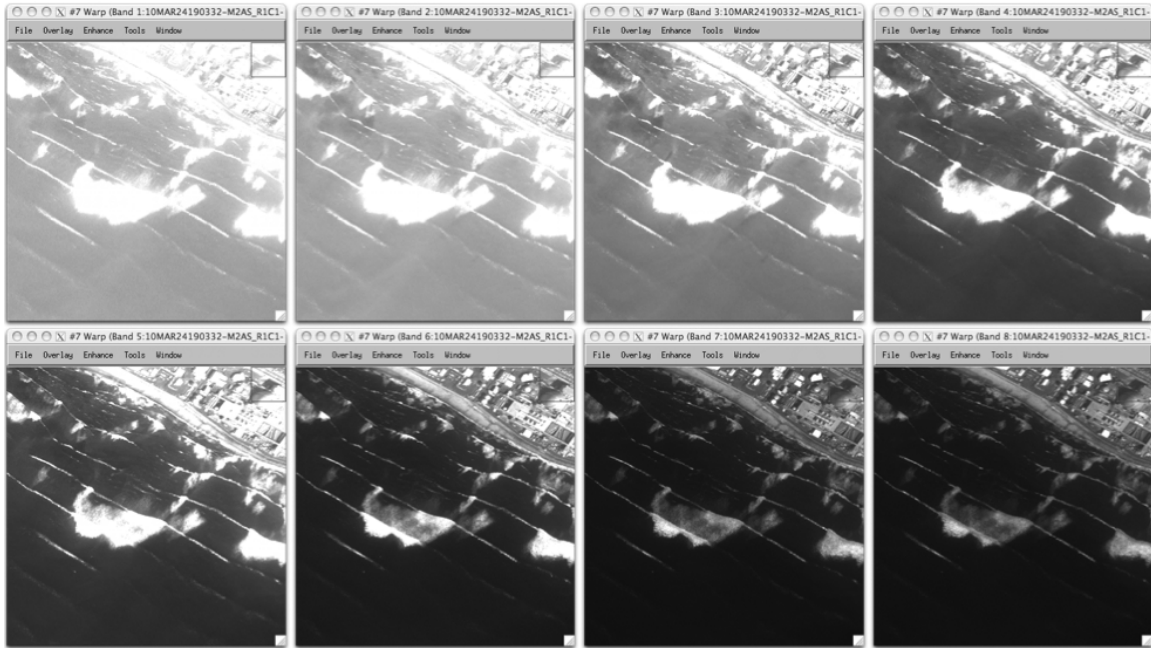


Figure 18. Original spectral bands one through eight example





Figure 19. Principal component bands one through eight example

Taking a transect of the inverse of the principal component four image shows high values corresponding to wave crest position. Figure 20 shows a transect of the principal component four image with transect profile.

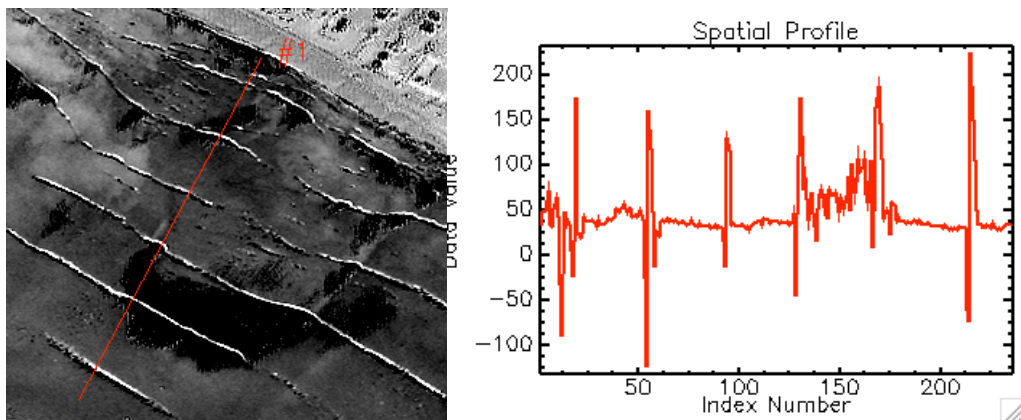


Figure 20. Principal component four inverse image with transect perpendicular to shore and profile

Once the principal components transform has been performed on each image, the waves in each image can be compared to each other. A new image can be displayed to show a change detection from the first image to the second image. Principal component four of the second image is placed into both the red and green inputs for an RGB triplet representation of the data. Principal component four of the first image is placed in the blue input.

Displaying the two images in this way allows visualization of the position of the visible waves in the two images as they change from the first image to the second image. Figure 21 shows the resultant change detection image. The blue lines represent the highlighted wave crests from principal component four in the first image. The yellow lines (the additive color combination of red and green) represent the highlighted wave crests from principal component four in the second image. The change detection image represents how the waves have moved from the first image to the second image in the time between the two images. The waves have moved from the blue line positions to the yellow line positions in time 10.80 seconds. This allows us to determine the change in wave position from one image to the next image in the time between images which gives us the wave celerity. The distance the wave moves from one image to the next was determined using the measurement tool in ENVI.

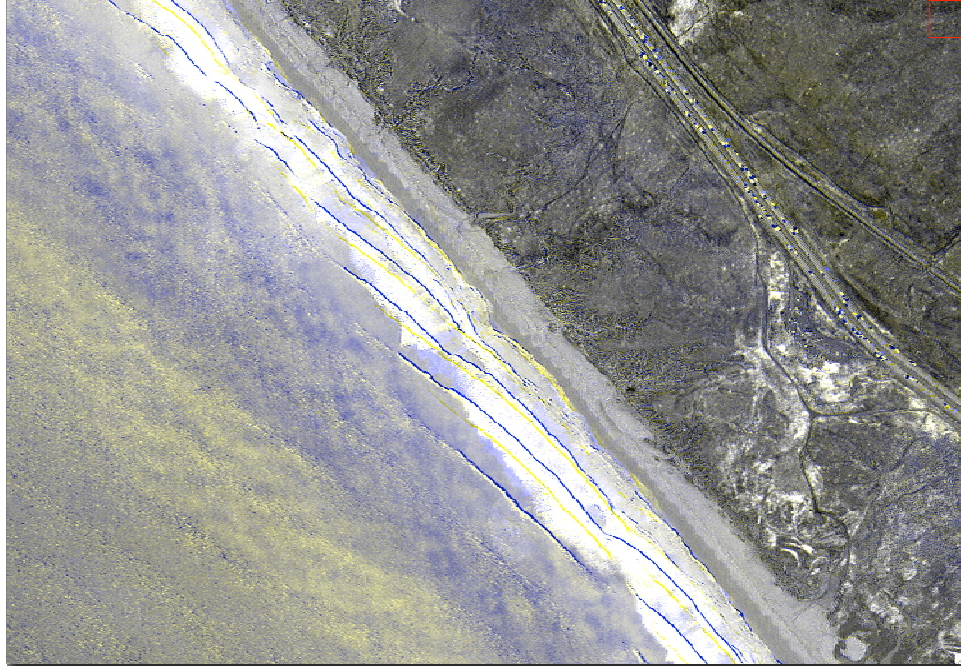


Figure 21. Change from first to second image where wave moves from blue to yellow toward the shore

We also looked at ways of highlighting several different scene components using the eight multispectral bands. Figure 22 shows part of the scene from image P002 row 1 column 1. The image was displayed with bands six, five, and three in an RGB triplet representation of the data. Several of the main components of the scene are highlighted including from left to right; waves, kelp (red), an airplane condensation trail, outflowing river sediment, and the shoreline (white).

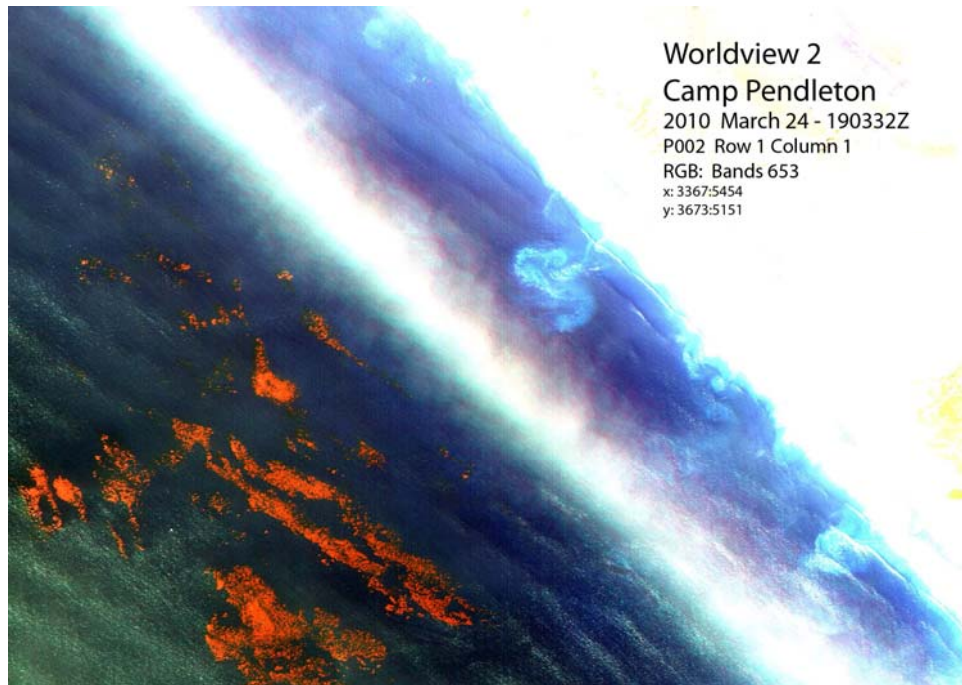


Figure 22. Illustration of Camp Pendleton scene components using multispectral data. Components of the scene highlighted include from left to right; waves, kelp (red), an airplane condensation trail, outflowing river sediment, and the shoreline (white)

Figure 23 shows the same scene using both multispectral and panchromatic image data. Principal component zero (intensity) from the multispectral image of P002 row 1 column 1 was compared to the panchromatic image of the same scene. In this image, the kelp (red) is now much better resolved because it is being represented with the panchromatic data which has approximately four times higher resolution. The principal component zero data shows the same features as in the previous figure, but the features are represented with different colors. Figures 22 and 23 are illustrations of our ability to separate scene components with the available image data.





Figure 23. Illustration of Camp Pendleton scene components using multispectral and panchromatic data

## B. WORLDVIEW-2 COLLECTION SIMULATION

A simulation of the Camp Pendleton area image collection was created using Satellite Tool Kit (from AGI). Figure 24 shows a movie of the collection simulation:

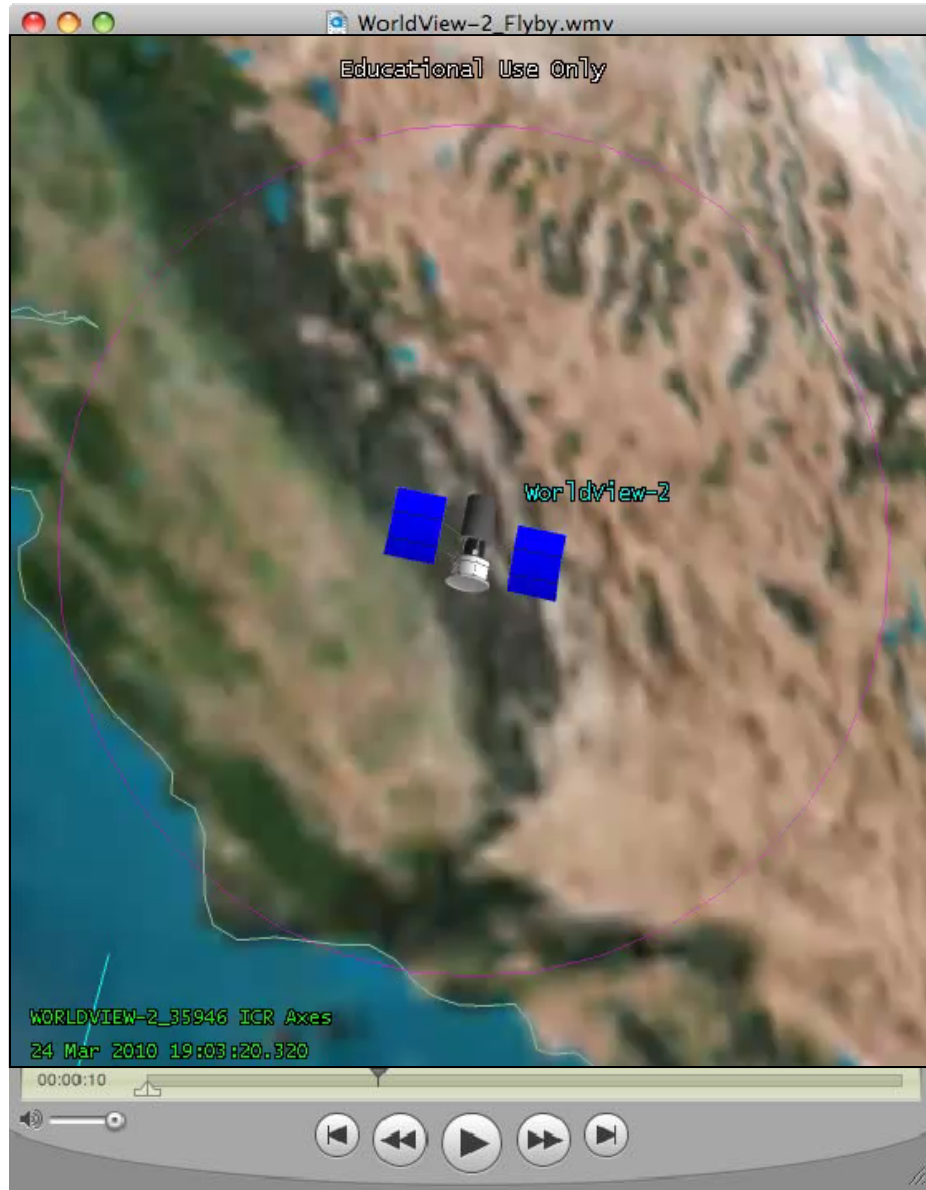


Figure 24. Satellite Toolkit simulation of WorldView-2 Camp Pendleton area collection

## V. ANALYSIS

### A. BATHYMETRY FROM IMAGERY

In order to determine depth relatively close to the shoreline using linear dispersion theory, we used the first three images in the data set. Each of the first three images (P002, P007, and P009) were registered to one of the middle images (P008). Principal component transforms were then computed for each co-registered image. Statistics were also calculated. Table 5 shows the computed statistics for the first image P002:

Table 5. Statistics of the first image computed during principal components transformation

Filename: /Users/blmccart/Documents/ENVI Data/10MAR24190332-M2AS_R1C1-052365928020_01_P002.TIF								
Dims: Full Scene (75,656,250 points)								
Basic Stats	Min	Max	Mean	Stdev	Num	Eigenvalue		
Band 1	0	1300	356.05	80.90	1	168,625.55		
Band 2	0	1499	300.95	75.65	2	27,243.87		
Band 3	0	2047	362.68	104.54	3	2,341.52		
Band 4	0	2035	277.79	97.06	4	222.48		
Band 5	0	1955	185.21	73.39	5	101.52		
Band 6	0	2047	396.04	185.39	6	89.68		
Band 7	0	2047	454.60	256.65	7	29.89		
Band 8	0	2047	431.48	245.80	8	7.85		
Covariance	Band 1	Band 2	Band 3	Band 4	Band 5	Band 6	Band 7	Band 8
Band 1	6,545.4	5,988.3	7,455.9	6,058.4	4,286.0	5,577.2	5,007.8	4,641.0
Band 2	5,988.3	5,722.3	7,437.6	6,260.3	4,548.6	5,412.7	4,583.0	4,205.3
Band 3	7,455.9	7,437.6	10,928.0	9,814.8	7,213.5	11,953.8	12,587.8	11,811.0
Band 4	6,058.4	6,260.3	9,814.8	9,421.3	7,049.1	12,194.9	13,013.0	12,328.0
Band 5	4,286.0	4,548.6	7,213.5	7,049.1	5,386.2	8,646.5	8,936.4	8,463.2
Band 6	5,577.2	5,412.7	11,953.8	12,194.9	8,646.5	34,370.4	46,489.9	44,520.5
Band 7	5,007.8	4,583.0	12,587.8	13,013.0	8,936.4	46,489.9	65,871.6	62,956.2
Band 8	4,641.0	4,205.3	11,811.0	12,328.0	8,463.2	44,520.5	62,956.2	60,417.1
Correlation	Band 1	Band 2	Band 3	Band 4	Band 5	Band 6	Band 7	Band 8
Band 1	1	0.98	0.88	0.77	0.72	0.37	0.24	0.23
Band 2	0.98	1	0.94	0.85	0.82	0.39	0.24	0.23
Band 3	0.88	0.94	1	0.97	0.94	0.62	0.47	0.46
Band 4	0.77	0.85	0.97	1	0.99	0.68	0.52	0.52
Band 5	0.72	0.82	0.94	0.99	1	0.64	0.47	0.47
Band 6	0.37	0.39	0.62	0.68	0.64	1	0.98	0.98
Band 7	0.24	0.24	0.47	0.52	0.47	0.98	1	1.00
Band 8	0.23	0.23	0.46	0.52	0.47	0.98	1.00	1
Eigenvector	Band 1	Band 2	Band 3	Band 4	Band 5	Band 6	Band 7	Band 8
PC Band 1	-0.069	-0.066	-0.148	-0.150	-0.105	-0.450	-0.619	-0.592
PC Band 2	0.417	0.416	0.511	0.436	0.330	0.053	-0.209	-0.214
PC Band 3	0.645	0.336	-0.014	-0.431	-0.467	-0.202	0.131	0.099
PC Band 4	-0.362	0.075	0.522	-0.085	-0.067	-0.506	0.522	-0.225
PC Band 5	0.206	0.042	-0.465	0.179	0.520	-0.599	0.202	0.194
PC Band 6	-0.185	0.020	0.335	-0.030	-0.067	-0.324	-0.487	0.711
PC Band 7	-0.130	0.275	0.068	-0.724	0.583	0.181	-0.071	-0.016
PC Band 8	0.426	-0.791	0.332	-0.192	0.207	-0.045	0.019	-0.020

The statistics show that bands 7 and 8 have very high covariance compared to the other covariance values. Figure 25 shows a plot of spectral band covariance values. Band to band correlation was also computed. Figure 26 shows a plot of spectral band correlation values.

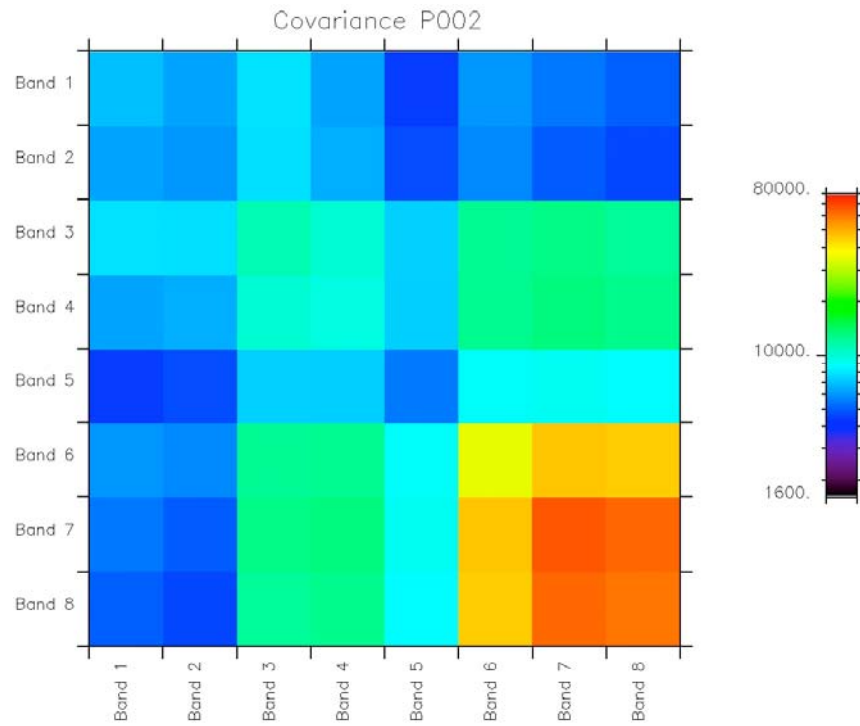


Figure 25. Covariance for the spectral bands of the first image

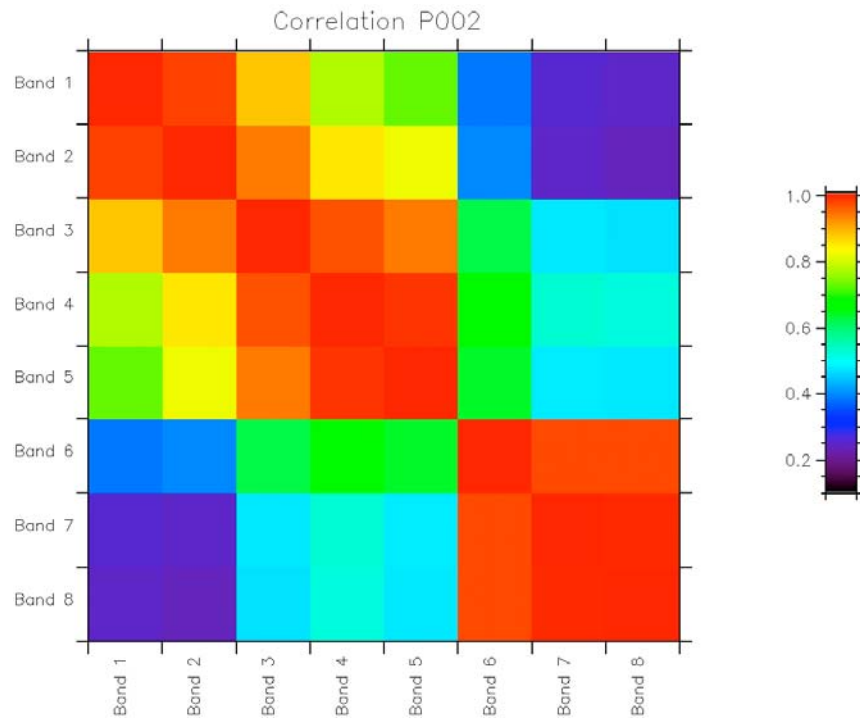


Figure 26. Correlation for the spectral bands of the first image



Eigenvector representations of each of the eight principal component bands are shown in Figures 27 and 28. Because the fourth principal component is best for highlighting wave crests and giving us wave position at a specific time, we were most interested in its eigenvector representation. Principal component four is highlighted in Figure 27. Principal component band 4 is composed of large parts of spectral bands three six and seven (Green, Red-Edge, and NIR1).

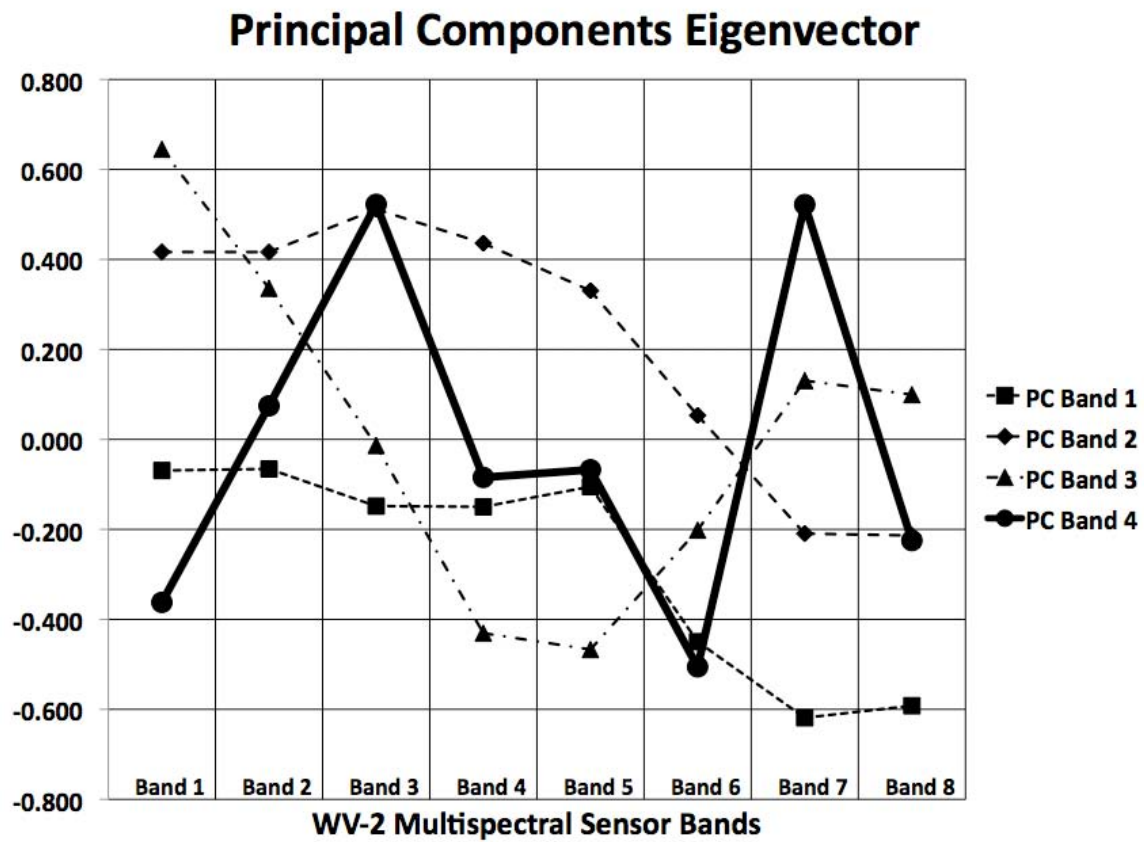


Figure 27. Eigenvector representation of principal component bands one through four with PC Band 4 highlighted

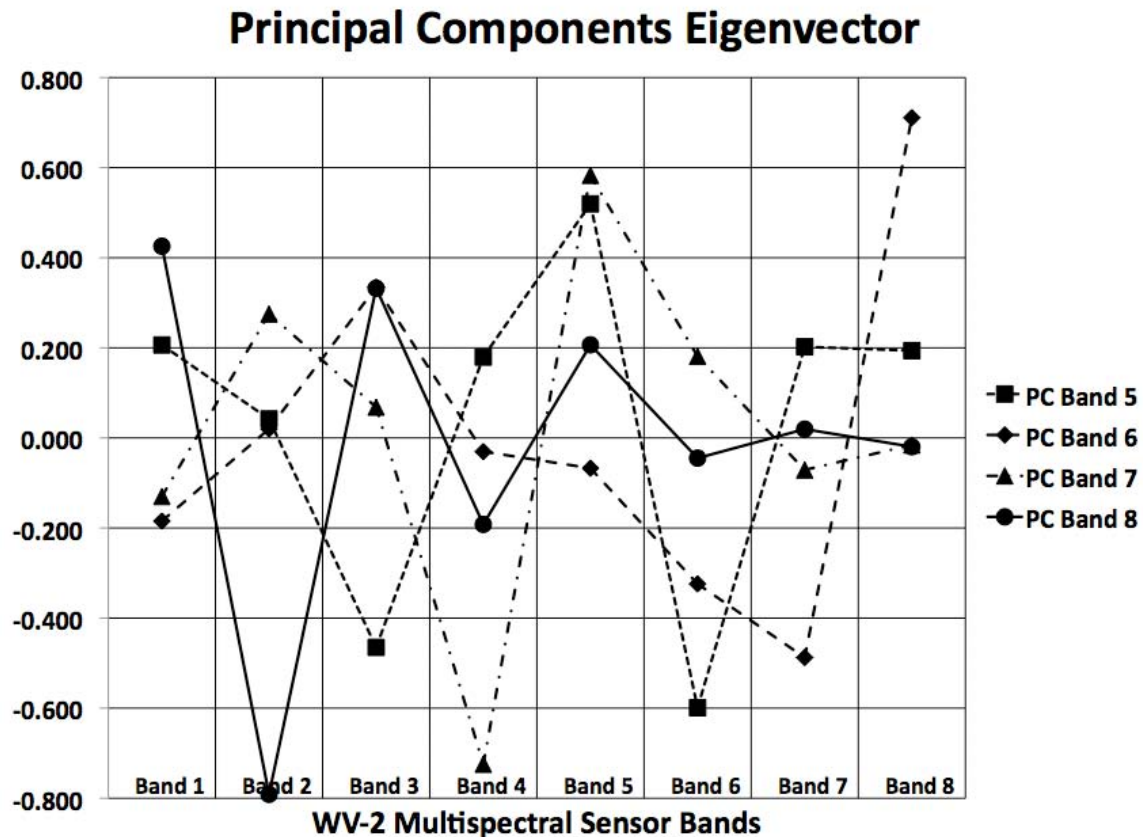


Figure 28. Eigenvector representation of principal component bands five through eight

Once principal component transforms had been computed for each co-registered image, they could be compared. A change detection image was created for the first two images. The change detection image was an RGB color composite with principal component four for the second image in the red and green components, and principal component four for the first image in the blue component.

In the change detection image, blue lines show the position of the wave in the first image, while yellow lines show the position of the waves in the second image. The waves move from their positions when they are blue to their positions when they are yellow in the time between the two images (10.80 seconds). Figure 29 shows a chip of this image. In the second change detection image, the waves move from their positions when they are blue to their positions when they are yellow in the time between the two images (also 10.80 seconds). Figure 30 shows a chip of this image.

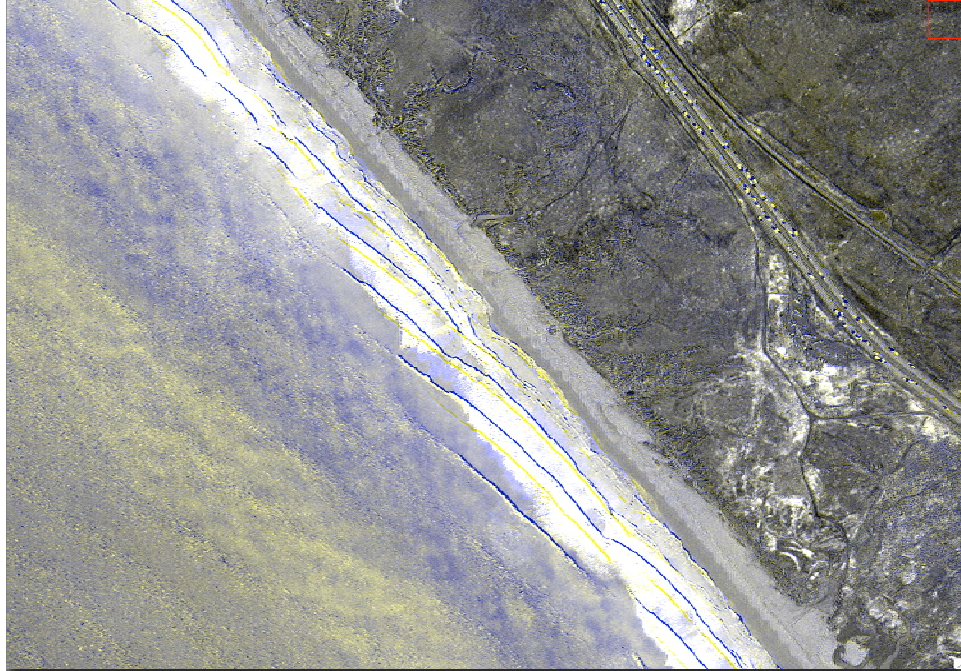


Figure 29. First image to second image change detection

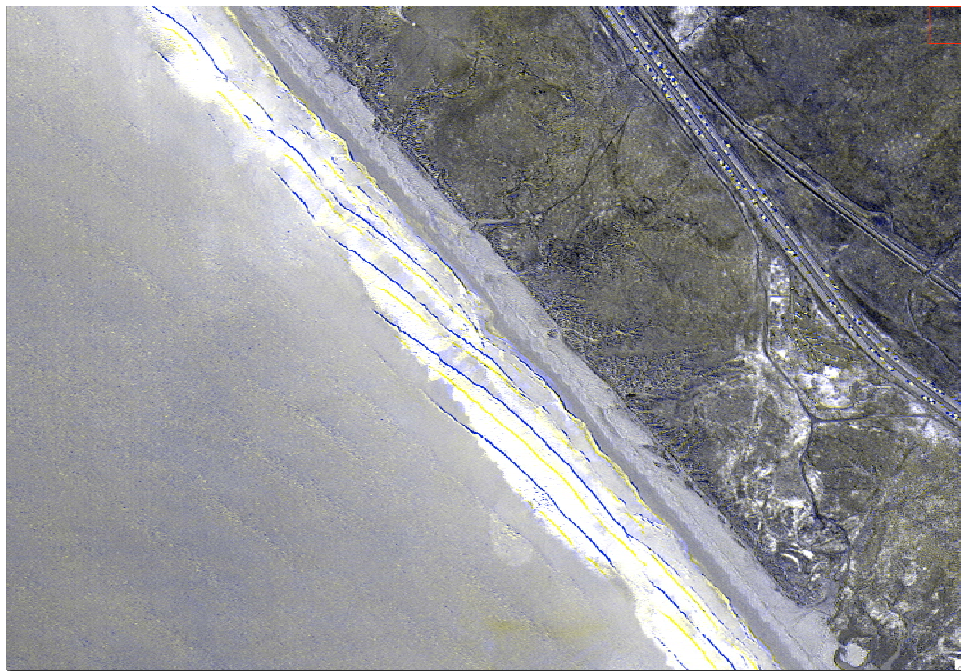


Figure 30. Second image to third image change detection



We were able to compare the two change detection images to each other as well. Another change detection image was created as an RGB color composite. The second of the original change detection images was used for red and green. The first of the original change detection images was used for blue. In this new change detection image waves move from cyan to magenta to yellow which are additive color combinations of the original red, green, and blue inputs.

Because the time delta between first and second images is the same as the time delta between second and third images, the lines lie directly on top of each other and the red, green, and blue inputs are all color mixed. That is why there are no red, green, or blue colors in the resultant image. Figure 31 shows a chip from the image. From the figure you can see that there is an additional yellow line between cyan and magenta. There is also an additional cyan line between magenta and yellow. These additional lines are caused by multiple waves overlapping. Multiple waves overlapping will cause more and more additional lines to appear as more data sets are combined in this way. Combining more than two sets of images in this way was not particularly useful.

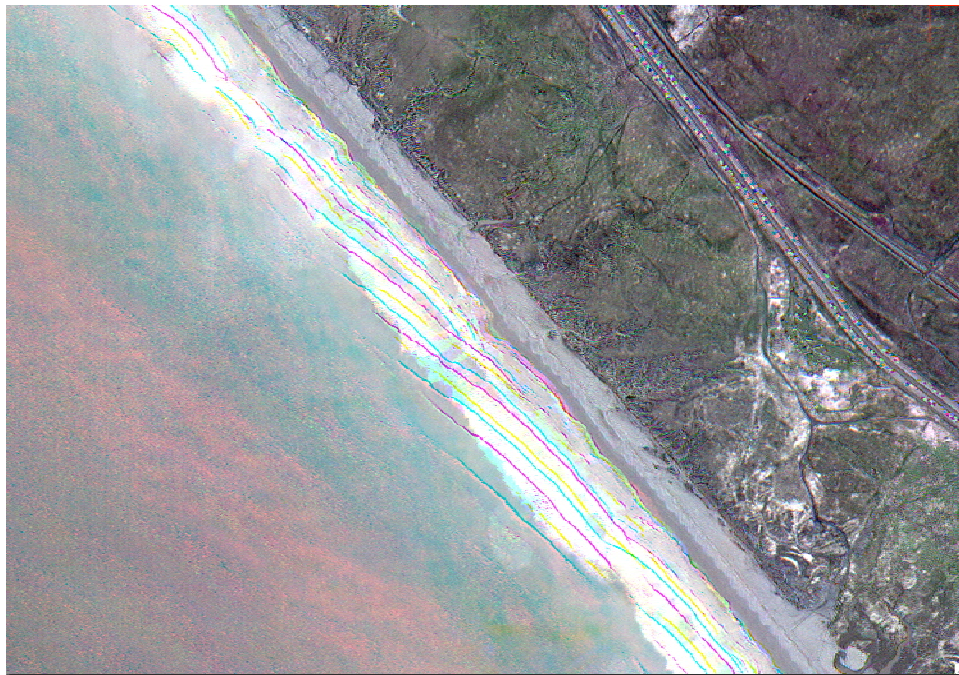


Figure 31. First to second to third image change detection showing only additive color mixed wave lines

The measurement tool in ENVI was used to measure the distance the wave travels. The depth of the water at the midpoint between the blue and yellow lines in the change detection image was determined using Equation 1 (Equation 4 can also be used). Water depth was determined in this way at points all along the shoreline in the change detection images.

Next, it was necessary to compare these computed depths to reference bathymetry. Maps were created of the Camp Pendleton area using ArcGIS software. The maps allowed accurate alignment of image data with reference bathymetry. The bathymetry used was created by ESRI and modified by the California Department of Fish and Game. The bathymetry consists of ten meter contour lines to six hundred meters depth. Figure 32 shows a chip from a change detection image placed in a map with bathymetry contour lines and sediment types.

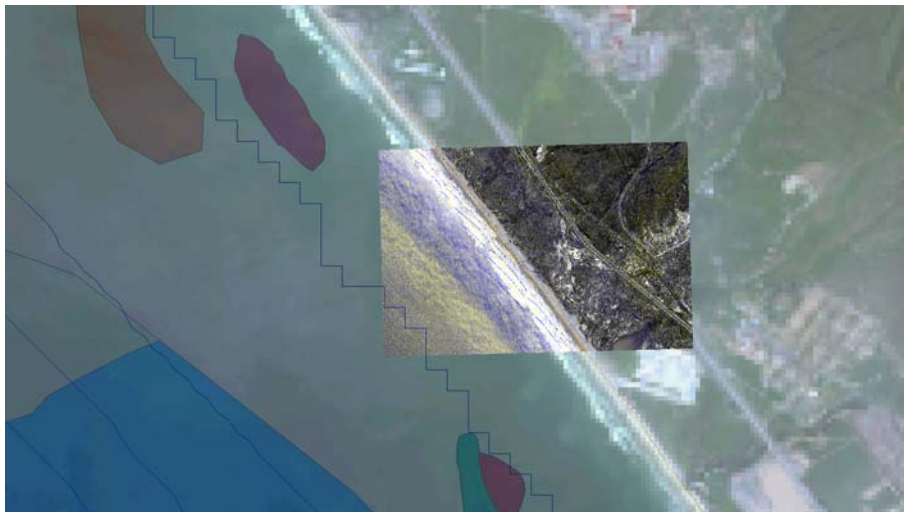


Figure 32. Overlay of surveyed bathymetry to depth measured change detection image

This process works well for the waves close to the shore (<1000 m from the shore) where principal component four is able to highlight the wave crests. For waves farther from shore (1000 m to 3000 m), principal component four is not able to highlight the wave crests. Another process must be used in order to determine depth farther from shore. The wave period method as described by Williams, 1947 was used for these waves.

Depth curves were created as a function of wave period and wavelength in order to perform the wave period determination of water depth. These were very similar to those produced by Williams, 1947 (see Figure 2). Because we were working in units of meters, a set of depth curves was created using units of meters and seconds. The figure was created to allow determination of depth from a single multispectral image of the Camp Pendleton area. Figure 33 shows a plot of depth curves as a function of period and wavelength. Wavelengths for waves occurring over known depth postings were measured using the ENVI measurement tool. Surface gravity waves maintain the same period as they propagate but their celerity and wavelength can change. Other wavelengths can then be measured and the same period assumed. The depth below other waves can be determined by which depth curve intersects the period and wavelength of the wave using Figure 33.

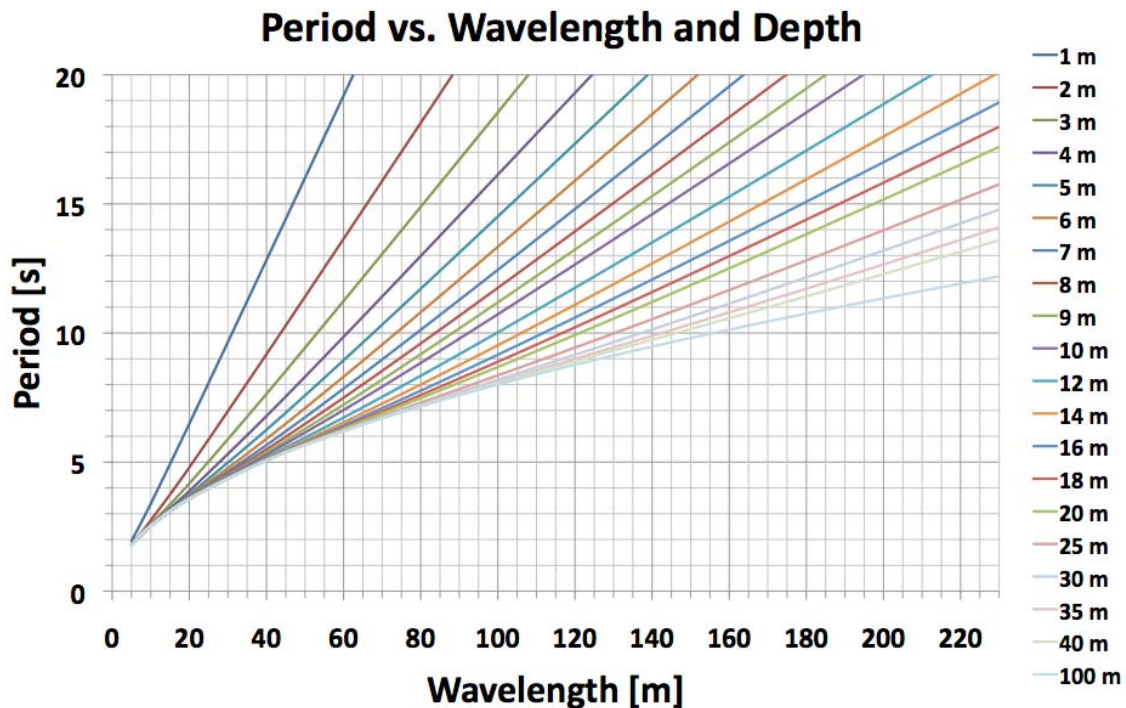


Figure 33. Curves relating wave period to depth and wavelength (wavelength units in meters)

The multispectral image data were represented in several different ways to see which representation could best highlight waves in a given image chip. Figure 34 shows



one representation using bands seven, six, and five in an RGB color representation of the data. These bands correspond to NIR1, Red-Edge, and Red bands. These bands do not penetrate the water, and this results in increased surface wave contrast (Abileah, 2006). Different band combinations and image enhancements were used depending on the particular image chip. Typically, image equalization enhancement did the best job of highlighting the waves in a given image chip.

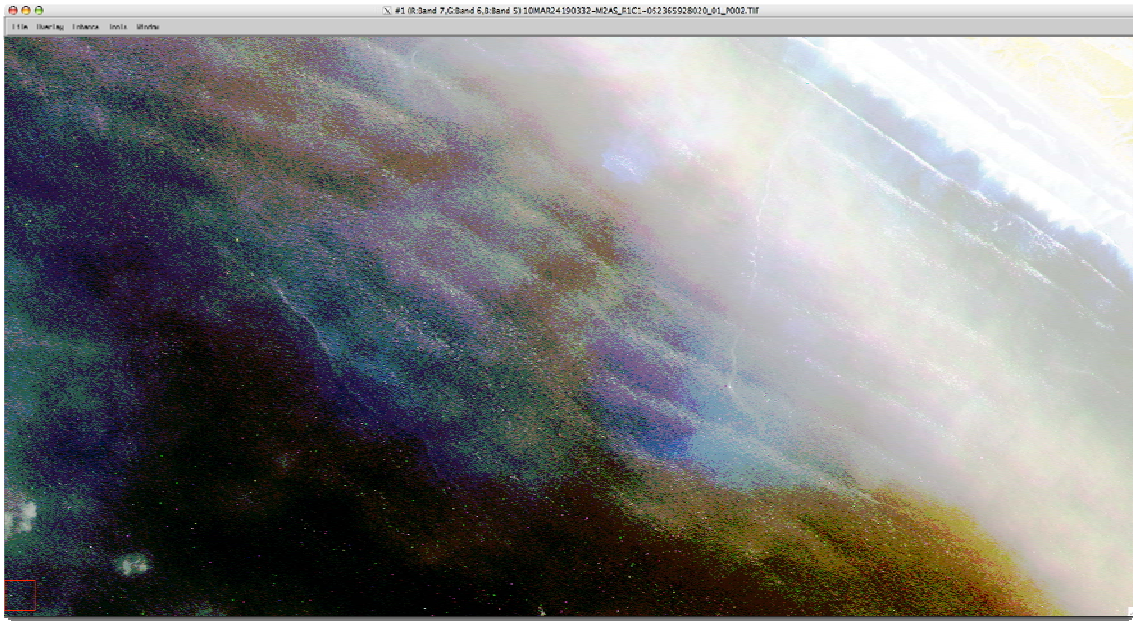


Figure 34. Deeper water waves resolved using 765 bands in RGB triplet representation

We now had two different methods of determining water depth from the Camp Pendleton area imagery. The first was to use co-registered sequential images transformed into their principal components. A single change detection image could then be created that showed the change in principal component four from the first image to the second. The depth below the halfway point between the two wave positions could be computed using the wave velocity method with the linear dispersion relation equation. This method works well for waves having a distance from shore of less than a thousand meters or so.

The second method uses a single multispectral image represented as an RGB color composite of three of the higher bands and equalization enhancement. The wavelength above a known depth can be used to determine wave period. Following the

same wave direction to shore we can assume the same period for other waves of differing wavelength. Using Figure 33, we can then determine depth for the other waves by measuring their wavelengths and assuming the same wave period.

## B. COMPARISON TO REFERENCE BATHYMETRY

The next step was to compare these calculated depths to our reference bathymetry. The WorldView-2 images used for this study were taken between 12:03 PM and 12:06 PM PDT. The National Oceanic and Atmospheric Administration operates coastal stations where tide levels are verified. The closest station to the Camp Pendleton area is in La Jolla around thirty miles south. The station identification number is 9410230. The NOAA website allowed determination of the verified water level on the day and time of image acquisition. Figure 35 shows a plot of water level versus time for March 24, 2010 at La Jolla, California.

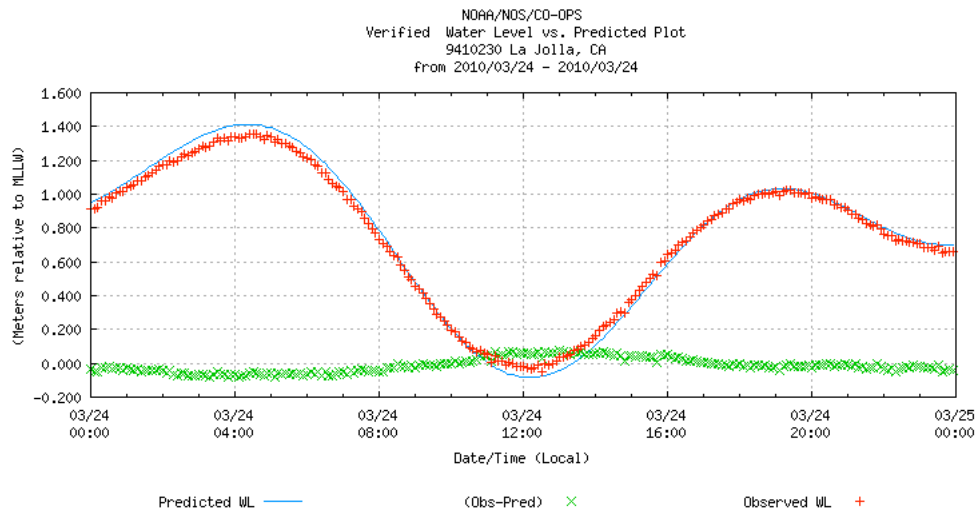


Figure 35. Tide height for March 24, 2010 at closest station to Camp Pendleton (From [National Oceanic and Atmospheric Administration, 2010, August 25])

Figure 35 shows that when the Camp Pendleton area images were acquired (12:03 to 12:06 PM PDT), the water level was very close to the mean low water level. Our reference bathymetry is also relative to mean low water level so there is no real water level offset that needed to be done to compare calculated depth to the reference bathymetry.



The first change detection image was carefully combined with the map layer containing the reference bathymetry. A perpendicular line was drawn on the image from the shoreline out into the water where it would cross as many contour lines as possible. Figure 36 shows the resultant image with perpendicular drawn to the shoreline. The ENVI measurement tool was used to measure from the shoreline to where each contour line crossed the perpendicular line. This produced a reference bathymetry depth profile curve.

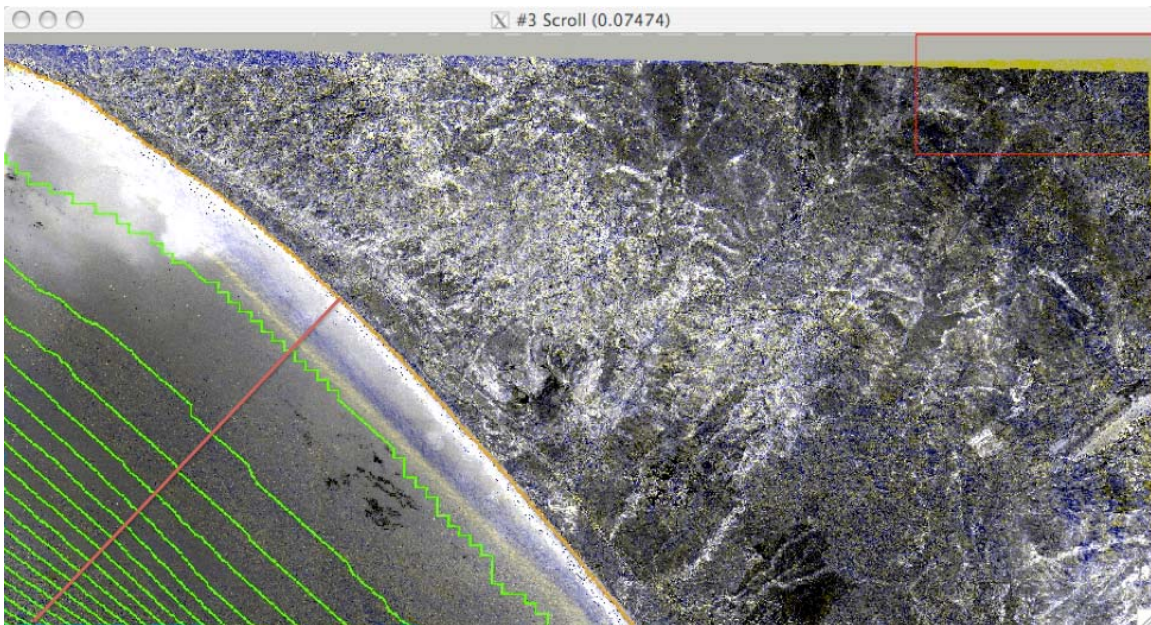


Figure 36. Bathymetric contours with perpendicular drawn to shoreline overlayed on top of change detection image

Once the reference bathymetry depth profile was determined, we determined depth for other waves along the perpendicular line. For waves less than about five hundred meters from the shoreline, the change detection image was used to determine depth using the wave velocity method. Only four points along the perpendicular line were measured since only four were easily distinguished in the image.

A multispectral image representation of the data was created in a new window and the two images were linked together using ENVI. In this way we were able to use the reference image containing the reference bathymetry and perpendicular line with a single image of the scene. The wavelength of a wave crossing the twenty meter depth

contour was measured and its period was determined from Figure 33. The wavelength of waves along the perpendicular line toward the shore were then measured and using the same period as the wave at twenty meters depth, the depths of the midpoint between the waves crests was determined. For each depth point, the distance to shore was determined using the ENVI measurement tool. Figure 37 shows the resultant depth profile.

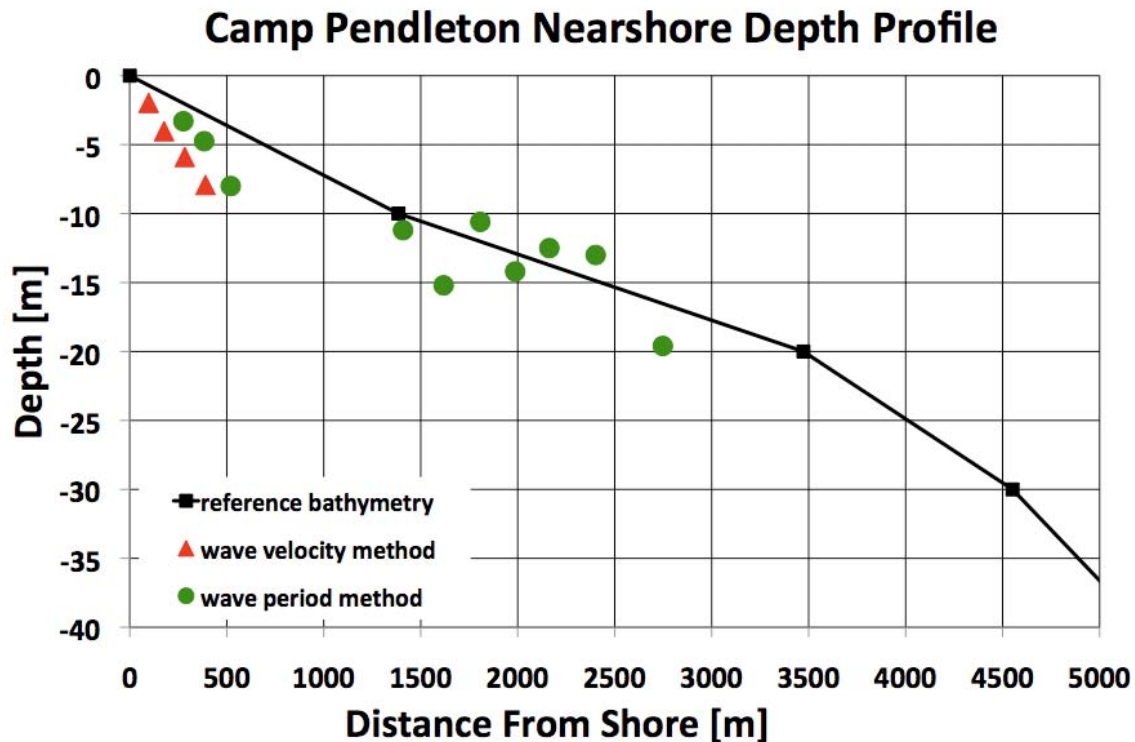


Figure 37. Nearshore depth profile with data points from wave velocity and wave period methods

The red triangles represent the data points determined through the use of the change detection image and the wave velocity method using the linear finite depth dispersion relation for surface gravity waves. The green circles represent the data points determined through the use of the wave period method using the linear dispersion relation. From about six hundred meters to twelve hundred meters from the shoreline, there is an airplane condensation trail which obscured the waves and we were not able to get depth data points in that area. For distances greater than about thirty five hundred meters from shore waves could not be very well resolved so we were not able to get depth data points beyond that point.

Using the linear dispersion theory has a maximum predicted error of 42% associated with not taking into account the non linearities (primarily the height of the waves) associated with surface gravity wave dispersion theory (Stockdon & Holman, 2000). The maximum predicted error results in an overprediction of water depth. Figure 38 shows the depth profile plot further zoomed in on the data points. The data points associated with the wave velocity method of depth determination have +42% error bars on them. The data points associated with the wave period method of depth determination have  $\pm 15\%$  error bars on them since they are farther from shore where the accuracy of the reference bathymetry should be higher. These error bars were used since they allowed most of the points greater than six hundred meters from the shore to intersect with the reference bathymetry line.

Depth accuracy of the data points is not readily apparent since the reference bathymetry has been linearly interpolated between the few data points available. Given the sparse reference bathymetry it is possible that our calculated depths are more accurate than the reference bathymetry. The bottom sediment composition in the nearshore area of this location consists primarily of fine sand and silt. Seasonal changes in ocean currents and tide levels, as well as severe storms could cause changes to depth because of the variable nature of the bottom sediments. It is possible that this could cause discrepancies between the reference bathymetry and the measured depths, especially in the surf zone. High resolution bathymetry (like high resolution imagery) necessarily equates to lower area coverage. In order to get higher resolution bathymetry covering the entire area in our scene, we would need to perform our own sonar bathymetric survey.

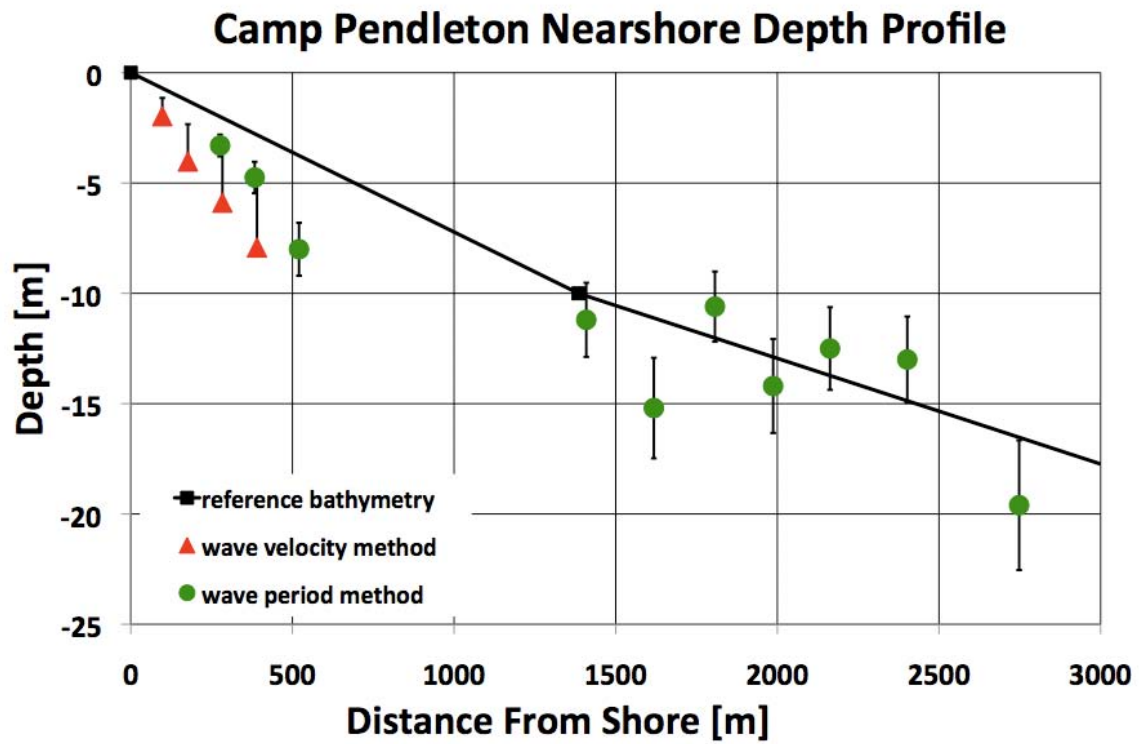


Figure 38. Nearshore depth profile with error bars (plus 42% for wave velocity, and plus/minus 15% for wave period)

## VI. SUMMARY

WorldView-2 multispectral imagery of the coastal area near Camp Pendleton, California were used to determine ocean depth using the linear finite depth dispersion relation for surface gravity waves. The high spatial resolution (fifty centimeters) available from the panchromatic imagery was not necessary for resolving waves since waves are much larger than this. The increased spectral resolution from the eight bands composing the multispectral imagery provided more degrees of freedom which could be used to perform the measurements.

The multispectral images were co-registered and principal component transforms were performed on them. Principal component four was found to very clearly highlight wave crests for waves within one thousand meters from shore. Creating a change detection image with principal component four for the second image represented by red and green, and principal component four for the first image represented by blue in an RGB triplet representation of the data produced a single image containing both spatial and temporal information. In the change detection image, waves moved from blue to yellow in the time between images. This allowed us to accurately measure the distance traveled by the wave in the time between images, which gave us wave celerity. Depth inversion of nearshore waves could be performed once wave celerity was known.

For waves between one thousand and thirty-five hundred meters from shore, another method for determining depth was needed since principal component four no longer highlighted wave crests in this region. The multispectral imagery was represented as an RGB composite image with longer wavelength bands and was equalization enhanced. This imagery allowed us to use the wave period method to determine ocean depth. The calculated depth data points were compared to reference bathymetry. Error bars of +42% were used on points determined with the wave velocity method. Error bars of  $\pm 15\%$  were used on points determined with the wave period method. Given the sparse reference bathymetry it is possible that our calculated depths are more accurate than the reference bathymetry, especially in the surf zone.

THIS PAGE INTENTIONALLY LEFT BLANK

## **VII. CONCLUSIONS AND FUTURE WORK**

Nearshore ocean depth was successfully determined using multispectral imagery acquired by the WorldView-2 satellite of the coastal area near Camp Pendleton, California. Image processing techniques were used to enhance wave position and allow measurement of wavelengths. Depth inversion was performed using both the wave velocity method and the wave period method. The computed depth data points compare favorably to reference bathymetry.

This work shows that it is feasible to use space-based multispectral sensors to determine nearshore ocean depth in denied waters where recent sonar bathymetric survey data are not available. The linear finite depth dispersion relation for surface gravity waves requires only that the top of the water waves can be resolved as opposed to the transparency method of depth determination.

Future work on this subject should involve an extensive high resolution sonar bathymetric survey of the coastal region in the scene of interest. This will allow better determination of computed depth accuracy when compared to recent high resolution bathymetry data.

The linear dispersion relation is capable of providing fairly accurate depth determination from space based imagery. The use of the non-linearity associated with wave height would increase the accuracy of depth inversion, but the wave trough to crest distance is very small compared to the wave to spacecraft distance. This may make it difficult to determine wave height from space.

The time interval between images should be closer to five seconds in order to increase accuracy without adversely affecting wave resolution. Because even a small amount of cloud cover will affect the ability to resolve waves, more images (twenty to thirty), should be taken of the same scene at five second intervals. Exhaustive depth computations using many images of the scene can be used to create a depth data point cloud along a depth profile line common to all images. This should help to establish the accuracy of this method.

THIS PAGE INTENTIONALLY LEFT BLANK



## LIST OF REFERENCES

- Abileah, R. (2006). Mapping shallow water depth from satellite. *Proceedings of the ASPRS Annual Conference. Reno, Nevada, May1-5, 2006.*
- Bell, P. S. (1999). Shallow water bathymetry derived from an analysis of x-band marine radar images of waves. *Coastal Engineering*, 37(1999), 513–527.
- Catalan, P. A., & Haller, M. C. (2008). Remote sensing of breaking wave phase speeds with application to non-linear depth inversions. *Coastal Engineering*, 55(2008), 93–111.
- Dalrymple, R. A., Kennedy, A. B., Kirby, J. T., & Chen, Q. (1998). Determining depth from remotely-sensed images. *Proceedings 26<sup>th</sup> International Conference on Coastal Engr. ASCE*, 2395–2408.
- DigitalGlobe, Inc. (2009). WorldView-2 imaging satellite. Longmont, Colorado: DigitalGlobe, Inc.
- DigitalGlobe, Inc. (2010a). DigitalGlobe core image products guide. Longmont, Colorado: DigitalGlobe, Inc.
- DigitalGlobe, Inc. (2010b). Whitepaper: The benefits of the 8 spectral bands of WorldView-2. Longmont, Colorado: DigitalGlobe, Inc.
- Dugan, J. P., Piotrowski, C. C., & Williams, J. Z. (2001). Water depth and surface current retrievals from airborne optical measurements of surface gravity wave dispersion. *Journal of Geophysical Research*, 106(C8), 16,903–16,915.
- Gao, J. (2009). Bathymetric mapping by means of remote sensing: methods, accuracy and limitations. *Progress in Physical Geography*, 33(1)(2009), 103–116.
- Holland, T. K. (2001). Application of the linear dispersion relation with respect to depth inversion and remotely sensed imagery. *IEEE Transactions on Geoscience and Remote Sensing*, 39(9), 2060–2072.
- ITT Visual Information Solutions. (2010). ENVI Tutorials. Boulder, Colorado: ITT Visual Information Solutions Corporation.
- Jackson, J. E. (2003). *A user's guide to principal components*. Hoboken, NJ: John Wiley & Sons.
- Kirby, J. T., & Dalrymple, R. A. (1986). An approximate model for nonlinear dispersion in monochromatic wave propagation models. *Coastal Engineering*, 9(1986), 545–561.

- Knauss, J. A. (1996). *Introduction to physical oceanography, second edition*. Upper Saddle River, NJ: Prentice-Hall.
- National Oceanic and Atmospheric Administration. (2010, August 25). *NOAA Tides and Currents*. Retrieved from NOAA Tides and Currents – Home website: <http://tidesandcurrents.noaa.gov/geo.shtml?location=9410230>
- Olsen, R. C. (2007). *Remote sensing from air and space*. Bellingham, WA: SPIE.
- Stockdon, H. F., & Holman R. A. (2000). Estimation of wave phase speed and nearshore bathymetry from video imagery. *Journal of Geophysical Research*, 105(C9), 22,015–22,033.
- Tripathi, N. K. & Rao, A. M. (2002). Bathymetric mapping in Kakinada Bay, India, using IRS-1D LISS-III data. *International Journal of Remote Sensing*, 23, 1013–1025.
- Williams, W.W. (1947). The determination of gradients on enemy-held beaches. *The Geographical Journal (The Royal Geographical Society)*, 109(1/3), 76–90.

## INITIAL DISTRIBUTION LIST

1. Defense Technical Information Center  
Ft. Belvoir, Virginia
2. Dudley Knox Library  
Naval Postgraduate School  
Monterey, California
3. Dr. Richard C. Olsen  
Naval Postgraduate School  
Monterey, California
4. Dr. Dan Boger  
Chair, Department of Information Sciences  
Naval Postgraduate School  
Monterey, California
5. Dr. Fred A. Kruse  
Naval Postgraduate School  
Monterey, California
6. Dr. Jamie MacMahan  
Naval Postgraduate School  
Monterey, California
7. Dr. Robert Arnone  
Naval Research Laboratory  
Stennis Space Center, Mississippi
8. Dr. Rikk Kvitek  
California State University, Monterey Bay  
Seaside, California
9. Ms. Khine Latt  
DARPA  
Arlington, Virginia
10. Mr. Ron Abileah  
jOmegaK  
San Carlos, California